

Deep Impact, Stardust-NExT and the behavior of Comet 9P/Tempel 1 from 1997 to 2010

K.J. Meech^{a,am,*,1}, J. Pittichová^{a,an}, B. Yang^b, A. Zenn^b, M.J.S. Belton^c, M.F. A'Hearn^d, S. Bagnulo^e, J. Bai^f, L. Barrera^g, J.M. Bauer^h, J. Bedientⁱ, B.C. Bhatt^j, H. Boehnhardt^k, N. Brosch^l, M. Buie^{m,1}, P. Candiaⁿ, W.-P. Chen^o, S. Chesley^p, P. Chiang^q, Y.-J. Choi^r, A. Cochran^s, S. Duddy^t, T.L. Farnham^{d,1}, Y. Fernández^u, P. Gutiérrez^v, O.R. Hainaut^w, D. Hampton^x, K. Herrmann^y, H. Hsieh^b, M.A. Kadooka^b, H. Kaluna^b, J. Keane^b, M.-J. Kim^z, J. Kley^{na}, K. Krisciunas^{aa}, T.R. Lauer^{ab}, L. Lara^v, J. Licandro^{ac}, S.C. Lowry^t, L.A. McFadden^{ad}, N. Moskovitz^{ae}, B.E.A. Mueller^{af,1}, D. Polishook^{ag}, N.S. Raja^b, T. Riesen^b, D.K. Sahu^j, N.H. Samarasingha^{af,1}, G. Sarid^b, T. Sekiguchi^{ah}, S. Sonnett^b, N. Suntzeff^{aa}, B. Taylor^{ai}, G.P. Tozzi^{aj}, R. Vasundhara^j, J.-B. Vincent^k, L. Wasserman^y, B. Webster-Schultz^{ak}, H. Zhao^{al}

^a Univ. Hawai'i, Institute for Astronomy, 2680 Woodlawn Drive, Honolulu, HI 96822, USA

^b Institute for Astronomy, 2680 Woodlawn Drive, Honolulu, HI 96822, USA

^c Belton Space Exploration Initiatives, LLC, 430 S. Randolph Way, Tucson, AZ 85716, USA

^d Univ. Maryland, Dept. of Astronomy, College Park, MD 20742, USA

^e Armagh Observatory, College Hill, Armagh BT61 9DG, UK

^f Yunnan Astronomical Observatory, Chinese Academy of Sciences, P.O. Box 110, Kunming 65011, Yunnan, PR China

^g Universidad Metropolitana de Ciencias de la Educación, Dep. Física, Avda. Jose Pedro Alessandri 774, Santiago, Chile

^h Jet Propulsion Laboratory, MS 183-301, 4800 Oak Grove Drive, Pasadena, CA 91109, USA

ⁱ University of Hawai'i, Honolulu, HI 96822, USA

^j Indian Institute of Astrophysics, II Block, Koramangala, Bangalore 560 034, India

^k Max-Planck Institut für Sonnensystemforschung, Max-Planck Str. 2, 37191 Katlenburg-Lindau, Germany

^l The Raymond and Beverly Sackler School of Physics and Astronomy, Tel Aviv University, 69978 Tel-Aviv, Israel

^m Southwest Research Institute, 1050 Walnut St., Suite 300, Boulder, CO 80302, USA

ⁿ Gemini Observatory, c/o AURA, Casilla 603, La Serena, Chile

^o Grad. Inst. of Astronomy, National Central Univ., 300 Jhongda Road, Jhongli 32001, Taiwan

^p Jet Propulsion Laboratory, MS 301-150, 4800 Oak Grove Drive, Pasadena, CA 91109, USA

^q National Central University, Jhongli City 320, Taiwan

^r Korea Astronomy and Space Science Institute, 776 Daedukdaero, Yuseong-gu, Daejeon 305-348, South Korea

^s Univ. Texas, Dept. Astronomy, 1 University Station, C1400, Austin, TX 78712, USA

^t Centre for Astrophysics and Planetary Science, School of Physical Sciences, The University of Kent, Canterbury CT2 7NH, UK

^u Univ. Central Florida, Dept. of Physics, 4000 Central Florida Blvd., Orlando, FL 32816-2385, USA

^v Instituto de Astrofísica de Andalucía – CSIC, Camino Bajo de Huétor 50, 18080 Granada, Spain

^w European Southern Observatory, Karl-Schwarzschild-Str. 2, D-85748 Garching bei München, Germany

^x Geophysical Institute, Univ. AK, 903 Koyukuk Dr., Fairbanks, AK 99775-7320, USA

^y Lowell Observatory, 1400 West Mars Hill Road, Flagstaff, AZ 86001, USA

^z Yonsei University, Dept. of Astronomy, 134 Sinchon-dong, Seodaemun-gu, Seoul 120-749, South Korea

^{aa} Dept. of Physics and Astronomy, Texas A&M Univ., College Station, TX 77843-4242, USA

^{ab} National Optical Astronomy Observatory, 950 N. Cherry Ave., Tucson, AZ 85719, USA

^{ac} Instituto de Astrofísica de Canarias, c/Vía Láctea s/n, 38200 La Laguna, y Dept. de Astrofísica, Universidad de La Laguna, E-38205 La Laguna, Tenerife, Spain

* Corresponding author.

E-mail addresses: meech@ifa.hawaii.edu (K.J. Meech), pittichova@ifa.hawaii.edu (J. Pittichová), yangbin@ifa.hawaii.edu (B. Yang), arzenn@ifa.hawaii.edu (A. Zenn), mbelton@dakotacom.net (M.J.S. Belton), ma@astro.umd.edu (M.F. A'Hearn), sba@arm.ac.uk (S. Bagnulo), baijinming@mail.ynao.ac.cn (J. Bai), luis.barrera@umce.cl (L. Barrera), bauer@scn.jpl.nasa.gov (J.M. Bauer), bedient@hawaii.edu (J. Bedient), bcb@iap.res.in (B.C. Bhatt), boehnhardt@mps.mpg.de (H. Boehnhardt), noah@wise.tau.ac.il (N. Brosch), buie@boulder.swri.edu (M. Buie), pcandia@gemini.edu (P. Candia), wchen@astro.ncu.edu.tw (W.-P. Chen), steve.chesley@jpl.nasa.gov (S. Chesley), pschiang@gmail.com (P. Chiang), yjchoi@kasi.re.kr (Y.-J. Choi), anita@barolo.as.utexas.edu (A. Cochran), S.Duddy@kent.ac.uk (S. Duddy), farnham@astro.umd.edu (T.L. Farnham), yan@physics.ucf.edu (Y. Fernández), pedroj@iaa.es (P. Gutiérrez), ohainaut@eso.org (O.R. Hainaut), dhampton@gi.alaska.edu (D. Hampton), herrmann@lowell.edu (K. Herrmann), hsieh@ifa.hawaii.edu (H. Hsieh), kadooka@ifa.hawaii.edu (M.A. Kadooka), kaluna@ifa.hawaii.edu (H. Kaluna), keane@ifa.hawaii.edu (J. Keane), skarma@galaxy.yonsei.ac.kr (M.-J. Kim), kleyna@ifa.hawaii.edu (J. Kley), krisciunas@physics.tamu.edu (K. Krisciunas), lauer@noao.edu (T.R. Lauer), lara@iaa.csic.es (L. Lara), jlicandr@iac.es (J. Licandro), S.C.Lowry@kent.ac.uk (S.C. Lowry), lucyann.a.mcfadden@nasa.gov (L.A. McFadden), nmoskovitz@dtm.ciw.edu (N. Moskovitz), muller@psi.edu (B.E.A. Mueller), david@wise.tau.ac.il (D. Polishook), raja@ifa.hawaii.edu (N.S. Raja), triesen@ifa.hawaii.edu (T. Riesen), dks@iap.res.in (D.K. Sahu), nalin@psi.edu (N.H. Samarasingha), sarid@ifa.hawaii.edu (G. Sarid), t.sekiguchi@nao.ac.jp (T. Sekiguchi), sonnett@ifa.hawaii.edu (S. Sonnett), nsuntzeff@tamu.edu (N. Suntzeff), bwtaylor@bu.edu (B. Taylor), tozzi@arcetri.astro.it (G.P. Tozzi), vasundhara.raju@gmail.com (R. Vasundhara), vincent@mps.mpg.de (J.-B. Vincent), lhw@lowell.edu (L. Wasserman), teacherschultz@hotmail.com (B. Webster-Schultz), meteorzh@pmo.ac.cn (H. Zhao).

¹ Visiting Astronomer, Kitt Peak National Observatory, and Cerro Tololo Ineramerican Observatory, National Optical Astronomy Observatory, which is operated by the Association of Universities for Research in Astronomy (AURA) under cooperative agreement with the National Science Foundation.

^{ad} Goddard Spaceflight Center, 8800 Greenbelt Rd., Greenbelt, MD 20771, USA

^{ae} Dept. of Terrestrial Magnetism, Carnegie Institution of Washington, 5241 Broad Branch Rd., Washington, DC 20015, USA

^{af} Planetary Science Institute, 1700 E. Ft. Lowell Rd., Suite 106, Tucson, AZ 85719, USA

^{ag} Dept. Geophysics & Planetary Sciences, Tel Aviv University, 69978 Tel-Aviv, Israel

^{ah} National Astronomical Observatory of Japan, 2-21-1 Osawa, Mitaka-shi, JP Tokyo 181-8588, Japan

^{ai} Lowell Observatory & Institute for Astrophysical Research, Boston University, 1400 W. Mars Hill Road, Flagstaff, AZ 86001, USA

^{aj} INAF – Osservatorio Astrofisico di Arcetri, Largo E. Fermi 5, I-50125 Firenze, Italy

^{ak} HAS, 47-728 Hui Kelu St. #9, Kaneohe, HI 96744, USA

^{al} Purple Mountain Obs., Chinese Academy of Sciences, 2# West Beijing Road, Nanjing 210008, PR China

^{am} NASA Astrobiology Institute, USA

^{an} Astronomical Institute of Slovak Academy of Sciences, Dúbravská cesta 9, 845 04 Bratislava, Slovak Republic

ARTICLE INFO

Article history:

Received 2 November 2010

Revised 12 February 2011

Accepted 14 February 2011

Available online 24 February 2011

Keywords:

Comet Tempel 1

Comets, Nucleus

Comets, Dust

Photometry

Ices

ABSTRACT

We present observational data for Comet 9P/Tempel 1 taken from 1997 through 2010 in an international collaboration in support of the *Deep Impact* and *Stardust-NExT* missions. The data were obtained to characterize the nucleus prior to the *Deep Impact* 2005 encounter, and to enable us to understand the rotation state in order to make a time of arrival adjustment in February 2010 that would allow us to image at least 25% of the nucleus seen by the *Deep Impact* spacecraft to better than 80 m/pixel, and to image the crater made during the encounter, if possible. In total, ~500 whole or partial nights were allocated to this project at 14 observatories worldwide, utilizing 25 telescopes. Seventy percent of these nights yielded useful data. The data were used to determine the linear phase coefficient for the comet in the R-band to be $0.045 \pm 0.001 \text{ mag deg}^{-1}$ from 1° to 16° . Cometary activity was observed to begin inbound near $r \sim 4.0$ AU and the activity ended near $r \sim 4.6$ AU as seen from the heliocentric secular light curves, water-sublimation models and from dust dynamical modeling. The light curve exhibits a significant pre- and post-perihelion brightness and activity asymmetry. There was a secular decrease in activity between the 2000 and 2005 perihelion passages of ~20%. The post-perihelion light curve cannot be easily explained by a simple decrease in solar insolation or observing geometry. CN emission was detected in the comet at 2.43 AU pre-perihelion, and by $r = 2.24$ AU emission from C₂ and C₃ were evident. In December 2004 the production rate of CN increased from $1.8 \times 10^{23} \text{ mol s}^{-1}$ to $Q_{\text{CN}} = 2.75 \times 10^{23} \text{ mol s}^{-1}$ in early January 2005 and $9.3 \times 10^{24} \text{ mol s}^{-1}$ on June 6, 2005 at $r = 1.53$ AU.

© 2011 Elsevier Inc. All rights reserved.

1. Introduction – cometary activity

1.1. The *Deep Impact* and *Stardust-NExT* missions and the Earth based observing campaign

1.1.1. The *Deep Impact* mission

On July 4, 2005, the two parts of the *Deep Impact* spacecraft made history as the first experiment to successfully probe beneath the surface of a comet nucleus. The impactor spacecraft performed as designed, colliding with the nucleus of 9P/Tempel 1 while the flyby spacecraft made unique *in situ* measurements. The geometry of the flyby limited us to imaging and near-infrared spectroscopy in an 800-s interval from the time of impact until the flyby spacecraft went into shield mode as it passed through the comet's orbital plane. After this period, at encounter plus 45 min, the spacecraft turned and looked back at the comet taking data of the impact trajectory back-lit by the Sun. A unique aspect of this mission was the observing program planned from Earth and Earth-orbit at the time of impact.

The selection of the *Deep Impact* mission target was driven by launch and orbital dynamics considerations, and not by the target properties. At the time of target selection, 9P/Tempel 1 was known to be a typical Jupiter-family low-activity comet (A'Hearn et al., 1995) rarely bright as seen from Earth, and was well placed for observing only every other apparition (~11 years). Although the comet was discovered in 1867 (Yeomans et al., 2005), there were relatively few physical observations of the comet prior to its selection for the *Deep Impact* mission. From the inclusion of the non-gravitational parameters in the orbit solution for the comet, it was suggested that the pattern of outgassing was relatively unchanged during the previous seven apparitions. Most of the existing physical observations were of the gas and dust coma around the time of the two perihelion passages of 1983 and 1994 (Lisse

et al., 2005), along with some limited information about the nucleus rotation (Lamy et al., 2001).

1.1.1.1. Pre-encounter characterization of 9P/Tempel 1. An intensive international Earth-based observing campaign was established in 1999 to provide critical inputs regarding the parameters of the nucleus to the mission planning team. The ground-based campaign had the further goals of characterizing the physical properties, activity and chemistry of the pre-encounter nucleus to facilitate the interpretation of the flyby spacecraft data, and establishing an activity baseline from which to look for impact induced changes (Meech et al., 2004). Knowledge of the nucleus size and albedo is important for the autonomous targeting software and in order to calculate instrument exposure times; in addition these are important parameters for interpreting activity with thermal models. These parameters were measured using combined optical measurements from the University of Hawai'i 2.2-m telescope and infrared measurements using the W. M. Keck Observatory (Fernández et al., 2003).

Implicit in using Earth-based optical and infrared measurements to estimate the nucleus size and albedo is an understanding of the surface scattering phase function, which can be obtained from observations of the inactive nucleus made over a range of phase angles. However, because the phase angle-related brightness changes can be comparable to the range of brightness variations induced by the changing scattering surface area as the comet rotates, the rotation light curve must be understood and removed in order to derive the phase function. The rotation state is a fundamental property of the nucleus, which can be used to derive constraints on the nucleus bulk strength and density. It is also important for thermal modeling and mission planning. Finally, understanding the onset of gas and dust production, and the dust environment at perihelion was important for assessing impact

hazards to the spacecraft, and encounter science interpretation. Belton et al. (2005) summarized the working properties of the nucleus derived from this campaign prior to encounter.

These measurements comprised the goals of the *Deep Impact* pre-encounter imaging campaign, which is reported here. During the few months leading up to encounter, the campaign widened in scope, encompassing most of the world's professional observatories, in a coordinated effort to explore the comet's activity on timescales and at wavelengths not possible with the *in situ* observations. The data utilized not only ground-based facilities but also Earth-orbital facilities, as well as other space resources. The specifics of the more extensive near encounter observations are discussed elsewhere (Meech et al., 2005).

1.1.1.2. *Deep Impact* encounter results. The *in situ* measurements of the comet revealed distinct morphologies (A'Hearn et al., 2005; Thomas et al., 2007) on a nucleus that was remarkably homogeneous in albedo and color (Li et al., 2007) with very limited exposures of water ice (Sunshine et al., 2006). The surface displayed regions with circular features with size distributions consistent with impact crater populations and in addition, two regions of smooth terrain were seen in regions of gravitational lows. These smooth terrains had characteristics of emplacement by flowing material (Thomas et al., 2007; Meech et al., 2008; Belton and Melosh, 2009). The nucleus was also distinctly layered, although *in situ* imaging was unable to ascertain the full extent of the layers. Analysis of the *in situ* thermal nucleus surface measurements yielded an extremely low thermal inertia (Groussin et al., 2007; Davidsson et al., 2007), which suggested that volatile materials were close to the surface.

On approach, many outbursts were detected, both from the ground (Lara et al., 2006; Lara et al., 2007), Earth orbit (Feldman et al., 2007) and from the spacecraft (A'Hearn et al., 2005), and analysis suggested at least two active areas (Farnham et al., 2007). Pre-impact *in situ* spectral imaging showed spatial compositional differences in the outgassed volatiles with water dominant at the subsolar point and CO₂ enhanced in the direction of the negative nucleus rotation pole (*i.e.* conventional Southern pole; Feaga et al. (2007)).

The impact event showed that the surface materials had negligible strength, and from following the ballistic trajectories of the ejecta, that the nucleus mean density was very low (Richardson et al., 2007). Ground-based spectra and *Spitzer* IR spectra showed that the dust grains de-aggregated into micron-sized grains from larger particles, and spectral signatures of a wide range of minerals from high temperature, crystalline olivine, to phyllosilicates that condense at lower temperatures were found (Farnham et al., 2007; Lisse et al., 2006). Additionally, there was some evidence of a different volatile chemistry from the material excavated from the impact (Mumma et al., 2005). The coma appearance returned to pre-encounter level and geometry within about a week after the impact event, displaying a porcupine jet pattern without any signature of continuing impact induced activity (Lara et al., 2007; Vincent et al., 2010).

1.1.2. The *Stardust-NExT* mission

After the successful completion of the *Deep Impact* mission, an extended mission opportunity to fly past the nucleus of Comet 9P/Tempel 1 was approved using the *Stardust* spacecraft. The mission's primary goals (level 1 requirements) were to image at least 25% of the terrain seen by *Deep Impact* at resolutions better than 80 m/pixel, including 7 high resolution images, and to image the crater made during the *Deep Impact* encounter if possible. The purpose of the extended investigation was to document surface changes between perihelia, to see if erosion is global, regional, or only in small active areas. By imaging both new and previously seen terrain, the

geologic mapping would be extended to assess if the layers seen during the encounter were global, and to see if there were additional regions of smooth flows. Finally, by imaging the crater it would be possible to see what a fresh crater looks like, including a search for ejecta preserved on the surface. Likewise, from the size of the crater it would be possible to make inferences about the mechanical properties of the surface materials.

When the extended mission was proposed, we knew that the rotation rate would need to be known to higher precision than previously measured in order to adjust the spacecraft time of arrival so that it would fly by the comet at the right time to see the crater. At the time of the mission confirmation, the extensive dataset obtained for *Deep Impact*, including the ground-based sets as well as the pre-encounter imaging as seen on approach from the spacecraft, suggested that the rate of rotation was changing. In order to meet the challenge of having an accurate enough rotational ephemeris to make a prediction (see paper II, Belton et al., 2011), international observing campaigns were planned by our team during the 2007–2009 observing seasons of the comet.

The data obtained for both the *Deep Impact* and *Stardust-NExT* campaigns from 1997 through the spring of 2010 when the comet went into solar conjunction are presented here, along with a discussion of the secular behavior of the comet, the development of activity and properties of the dust coma. This paper will serve as the record of one of the most extensive datasets ever collected on one comet, and will provide the background information for several analysis papers to follow on these data. These data are being prepared for ingestion into the Planetary Data System archive. An analysis of the comet rotation based on this dataset and a prediction for the rotational phase at the *Stardust-NExT* encounter to occur on 14 February 2011 is presented in Belton et al. (2011).

2. Observations

2.1. Coordinating the observations

The initial comet observing campaign began as requests for telescope time through telescope allocation committees to which a few of the mission co-investigators had access, namely through the facilities on Mauna Kea and through the National Optical Astronomy Observatory. Approximately two years before the encounter, a series of workshops were organized both in conjunction with international meetings and as small 1–2 day meetings at locations accessible to ground-based observers. These events are summarized in Table 1. At each of the meetings, the mission goals and mission design were presented, as well as what contributions from Earth-based observing were required for the interpretation of the *in situ* observations. The workshops fostered discussions between observers that allowed the community to assess which facilities could optimally provide specific datasets. From these efforts we built an interconnected network of observers providing input to the mission team and to each other in the months leading up to the encounter, and during the encounter.

The pre-encounter communication was via email and password-protected websites. The website was also used to share text useful for observing proposal development to secure telescope time. During the encounter week, additionally, we had real-time communication through a multi-port Polycom connection which enabled all the major observatories to meet daily.

2.1.1. Database development

In order to facilitate access to the growing amount of *Deep Impact* ground-based imaging, we designed and developed a relational database using IBM's DB2 database management system,

Table 1
Observing coordination events.

Location	Date	Location	Date
DPS, Monterey, CA	9/01/03	MacQuarie Univ., Australia	9/06/04
ESO Garching, Germany	2/14–15/04	AAS, Denver, CO	5/30/04
NOAO, KPNO, Tucson, AZ	2/23/04	Bioastronomy, Iceland	7/09/04
IfA, Hilo HI	4/03/04	COSPAR, Paris	7/20/04
Nat. Central Univ., Taiwan	5/28/04	AAS, San Diego	1/13/05
NOAO, CTIO, Chile	6/24/04		

Notes: DPS = Division for Planetary Sciences Meeting; ESO = European Southern Observatory; NOAO = National Optical Astronomy Observatory; IfA = Institute for Astronomy, Univ. Hawai'i; AAS = American Astronomical Society semi-annual meeting; COSPAR = Committee on Space Research.

which can be queried using a web interface developed in ColdFusion MX.

In its current form, the database contains reduced data products (photometry) from the ground-based CCD imaging program. Routines developed in *Perl* are used to parse the text files containing reduced data and insert the data into the database. Full information about the observations obtained on each night, including information about the observers and observing conditions, seeing, the instrument and telescope used (along with filter transmission curves and CCD quantum efficiencies) are stored in the database. Each observation is also tagged with the instantaneous values of

the heliocentric and geocentric distances (r and Δ) and phase angle (α), as well as the Sun-centered and Earth-centered state vectors. These values are obtained automatically by communicating with the Jet Propulsion Laboratory Solar System Dynamics ephemeris routines when new data are uploaded to the database.

This *Deep Impact* database can be queried using a web interface. The returned data can be sorted on several key parameters, such as date, time, filter, photometry aperture, by telescope, observer or instrument, and returned as either an HTML table, tab-delimited dataset, an Excel spreadsheet or CSV file format.

A network-attached storage system, with 4.3 Terabytes of usable disk space plus backup, is operational. It is intended to accommodate the expansion of the *Deep Impact* database to include images in addition to the currently-stored reduced data products, as well as reduced and image data for other comets. Other planned database enhancements include additional indexing and query optimization in order to improve response time for typical queries.

2.2. Circumstances of the observations

A summary of the telescopes, detectors and instrument specifications for all of the runs is given in [Tables 2 and 3](#) the observing geometry, conditions, filters, and number of images for each observing night with useful data are provided in a table in the [Supplementary material](#). Data were obtained on ~500 nights utilizing 25 telescopes around the world (see [Fig. 1](#)). The entire multi-color set encompasses ~5000 images. The photometry set is too massive to include

Table 2
Instrument specifications.

UT date range, mm/dd/yy	Code ^a	λ^b	ϕ^b	Telescope ^c	Instrument	RN (e ⁻)	Gain (e ⁻ /ADU)	Scale (" pix ⁻¹)
10/20/00	493	2:32:45	+37:13:25	Cal3.5m	LAICA	6.0	2.0	0.225
09/27/09	493	2:32:45	+37:13:25	Cal2.2m	CAFOS	5.1	2.3	0.53
09/19/01–11/15/01	097	34:45:45	+30:35:44	Wise1.0m	SITE	5.9	1.1	0.884
10/19/06–01/26/09	HCT	78:57:51	+32:46:46	HCT2.1m	HFOSC	4.8	1.22	0.296
12/15/09–12/18/09	286	102:47:17	+25:01:31	Yunnan2.4m	CCD	2.84	1.0	0.215
12/18/09–12/19/09	D29	118:27:50	+32:44:04	PMO1m	CCD	6.0	1.0	1.705
10/12/01–11/17/09	344	128:58:35	+36:09:53	BOAO1.8m	CCD	7.0	1.8	0.34
5/25/05–07/28/05		147:25:57	–42:50:50	Canopus1.0m	SITe512	7.9	2.2	0.434
07/03/05–07/12/05	568	204:31:40	+19:49:34	CFHT	MegaCam	3.0	1.67	0.187
08/19/07–11/21/07	568	204:31:40	+19:49:34	GeminiN8m	GMOS	7.2	5.25	0.073
11/24/97–06/08/05	568	204:31:40	+19:49:34	Keck10m	LRIS	6.4	2.04	0.215
11/21/97–06/09/10	568	204:31:40	+19:49:34	UH2.2m	Tek2k	6.0	0.74	0.219
08/02/00	568	204:31:40	+19:49:34	UH2.2m	8kMos	5–20	2.0	0.260
10/29/08–10/30/08	675	243:08:15	+33:21:15	Pal5.0m	LFC	11	2.0	0.182
09/21/01–11/01/02	695	248:24:19	+31:57:32	KPNO2.1m	T2KA	4.0	3.6	0.305
09/23/06–11/27/06	695	248:24:19	+31:57:32	KPNO2.1m	F3KB	7.5	2.3	0.19
11/21/09–12/21/09	695	248:24:19	+31:57:32	KPNO2.1m	T2KB	4.0	3.1	0.305
10/22/03–10/09/07	695	248:24:19	+31:57:32	KPNO4m	MOSA	5.8	3.2	0.26
09/28/00–12/19/09	688	248:27:52	+35:05:46	Low1.8m	PRISM	6.9	2.6	0.39
08/26/00–11/03/00	711	255:58:43	+30:40:18	McD0.8m	PFcam	5.9	1.60	1.355
12/05/01	711	255:58:43	+30:40:18	McD2.1m	IGI/TK4	4.2	2.65	0.572
09/21/01–02/07/02	711	255:58:43	+30:40:18	McD2.7m	WHT-SITe	4.4	2.8	0.48
12/30/03–12/31/03	807	289:11:39	–30:10:09	CTIO4m	MOSAICII	3.5	1.5	0.432
11/10/01–11/12/01	807	289:11:39	–30:10:09	CTIO1.5m	Site2K6	3.7	2.0	0.048
10/20/00–10/23/00	809	289:16:13	–29:15:26	Dan1.5m	LORAL	7.7	1.37	0.39
05/06/00–11/27/00	809	289:16:13	–29:15:26	ESO2.2m	WFI	4.8	1.93	0.238
12/29/03–10/24/06	809	289:16:13	–29:15:26	ESONTT	EFOSC2	9.0	1.3	0.12
10/25/97	809	289:16:13	–29:15:26	ESONTT	EMMI/TKEB4	5.2	2.33	0.27
01/01/04–12/31/06	309	289:35:48	–24:37:32	VLT8m	FORS2	6.0	3.2	0.25
10/15/07–10/16/07	950	342:07:03	+28:45:37	WHT4.2m	PFIP	6.0	3.0	0.24
09/05/00–02/04/02	950	342:07:03	+28:45:37	TNG3.6m	OIG	4.0	1.6	0.277
11/13/09–11/15/09	J13	342:07:03	+28:45:37	LiverT2.0m	RATCam	5.0	2.34	0.135

^a Observatory code.

^b East longitude and geocentric latitude.

^c Telescope abbreviations: BOAO = Bohyunsan Optical Astronomy Observatory, Cal = Calar Alto, CFHT = Canada–France–Hawai'i Telescope, CTIO = Cerro Tololo Inter-American Observatory, Dan = Danish 1.5 m at ESO La Silla, ESO = European Southern Observatory, HCT = Himalayan Chandra Telescope, JCMT = James Clerk Maxwell Telescope, KPNO = Kitt Peak National Observatory, LiverT = The Liverpool Telescope, Low = Lowell Observatory, McD = McDonald Observatory, NIT = New Technology Telescope, Pal = Palomar Observatory, PMO = Purple Mountain Observatory, TNG = Telescopio Nazionale Galileo, UH = Univ. Hawai'i, VLT = ESO Very Large Telescope, WHT = William Herschel Telescope.



Fig. 1. Google maps image of the locations of the telescope facilities collaborating for this project.

in this paper in table form. In addition to submitting all of the data to the PDS, we are expanding the web-accessible database with the intention of making public all of the intermediate ancillary products associated with this paper, *e.g.* the photometry files, composite images, models. This archive and web access will be discussed in a separate paper.

All of the images were taken through the Kron–Cousins V ($\lambda_{\text{eff}} = 5473 \text{ \AA}$, $\Delta\lambda = 1185 \text{ \AA}$) and R ($\lambda_{\text{eff}} = 6417 \text{ \AA}$, $\Delta\lambda = 948 \text{ \AA}$) filters, were guided at non-sidereal rates, and calibration standard star measurements were taken from the Landolt (1992) star fields, unless otherwise noted. For all observing runs, flatfield calibrations were obtained during the evening and morning twilights unless otherwise noted.

Observing runs dedicated to calibration were carried out at Mauna Kea UH2.2-m (February 2000 and fall 2009) and the CTIO1.3-m telescopes. The calibration process places all of the data from different telescopes around the world on a single photometric system. Good photometric conditions were required for these runs. As a consequence, data acquired at observatories under non-photometric conditions are calibrated but have somewhat higher measurement errors. The data reduction is discussed below and in Section 2.3. The calibration of the non-photometric data used differential photometry with a large number of field star measurements (20–50) for each CCD image. Brief synopses of the observing runs (in alphabetical order by observatory), remarking in particular

on anything that could affect the data quality are included in the [Supplementary material](#).

2.3. Data reduction

2.3.1. Flattening, calibration, and dispersion correction

2.3.1.1. Imaging. Where possible, flat field images were obtained on the twilight sky for each of the filters and were used with bias frames to flatten the data in a standard manner. There were some datasets where weather conditions or instrument problems prevented the acquisition of flat fields, and for these sets we used either flats from adjacent nights or used the images themselves to create deep sky flats by median combining the images to create a blank sky field from which a correction to the pixel to pixel response could be made from higher S/N images from another night.

2.3.1.2. Spectra. The Keck data were reduced using the Image Reduction and Analysis Facility (IRAF) software package. All images were bias-subtracted and flat fielded. Cosmic-rays in the scientific frames were removed by *cosmic-ray* routine. However, some bright residuals were marked by eye and replaced by interpolating from adjacent pixels. Wavelength calibration was accomplished using the HgZnCd internal calibration lamps. After wavelength calibration, a standard atmospheric extinction curve for the Keck Observatory was used to calibrate atmospheric extinction. Finally, the

spectra of the comet and the solar-analog stars were flux calibrated from observing nearby spectrophotometric standard stars.

2.3.2. Aperture photometry

Fluxes were extracted using the IRAF *apphot* package (Tody, 1986). The aperture radius used was typically selected to encompass all of the light of the bare nucleus within the limit of the photometric errors (typically, this was a radius twice that of the seeing, see the table of observing conditions in the [Supplementary material](#)). For the runs where the comet was active, we typically measured through multiple apertures, but for the analysis presented here, used the data obtained through the 5.0" radius aperture. For the standard stars, apertures were selected from curves of growth determined on each night so that 99.5% of the light was

contained within the aperture. Because of the large size of the detectors, we typically had over 100 standard star measurements on each photometric night, taken over a range of airmasses and colors, thus ensuring an absolute calibration to a few percent. Fig. 2 shows the normalized standard star fluxes (Δmag) versus airmass, and the terms in the transformation to a standard photometric system for all the Mauna Kea data taken during December 2009 illustrating the stability of the site. Most of the runs were cross calibrated on these nights to put them on the same photometric system.

The comet was typically faint, and during the course of each night passed over faint background galaxies and field stars. In order to remove this extra flux from the photometry aperture when the comet was a point source, we created composite star images to

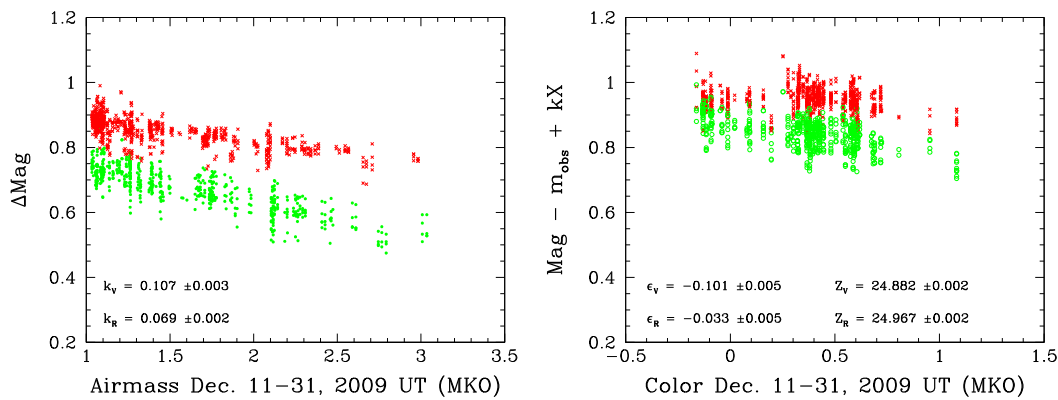


Fig. 2. [Left] Mauna Kea extinction coefficient, k_i (mag/airmass), in R filter (red crosses) and V filter (green circles) for the nights of 11–31 December 2009 obtained during the evening and morning twilights. [Right] Transformation coefficients (yielding color term, ϵ_i , and zero point, Z_i) for the R filter (red crosses) and V filter (green circles) for the same dates. Both plots illustrate the excellent site stability at Mauna Kea for photometric transformations. (For interpretation of the references to color in this figure legend, the reader is referred to the web version of this article.)

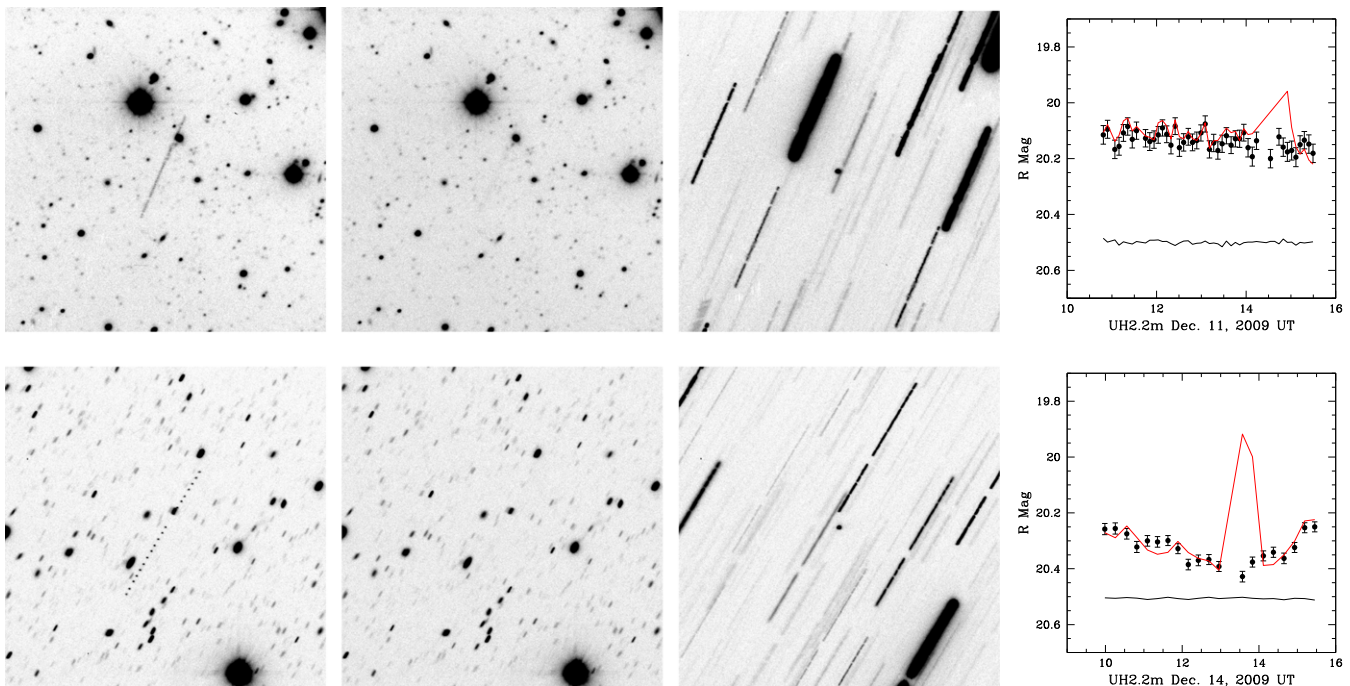


Fig. 3. Illustration of the technique used to extract light curves. The upper row corresponds to data from the UH2.2-m telescope obtained 11 December 2009, and the bottom row from the same facility on 14 December 2009. Left to right: (i) Composite image made by adding together all of the night's data. (ii) Composite image made by median combining the night's data. (iii) Composite image stacked to remove the non-sidereal motion of the comet. (iv) Comet light curve. Data points represent the final background-subtracted curve; red line represents the light curve before background subtraction. Horizontal black line shows the average of field stars of comparable magnitude to the comet, illustrating the stability of the differential photometry. (For interpretation of the references to color in this figure legend, the reader is referred to the web version of this article.)

be subtracted from the individual frames. As many field stars as possible (e.g. good S/N , and not saturated) were measured in each image (typically 30–100 stars). The centroid positions of all the field stars in the first frame were compared with the centroids for the same stars in each subsequent frame to compute a precise $(\delta x, \delta y)$ shift relative to the first frame (caused by guiding errors, non-sidereal guiding, and dithering). The frames were then all shifted to align with the first frame and median combined using mode scaling and cosmic-ray rejection. This resulted in a deep master star image where the moving comet was removed (see Fig. 3 for examples from 11 and 14 December 2009). On nights when the seeing was variable, the images were stacked and subtracted in batches of similar seeing. The composite images were scaled to the exposure time of the individual frames and subtracted from each frame to remove background field stars and galaxies. Photometry was then performed on the background-subtracted images.

The differential offsets were also used to create composite images for the runs. Representative images are shown in Figs. 4–7 as the heliocentric distance changed, illustrating the development and disappearance of the coma and tail. The parameters of all the images are listed in Table 4.

2.3.3. Differential photometry

In order to produce light curves on a single, uniform photometric system from multiple telescopes, we re-calibrated all fields obtained at other observatories with data from the UH2.2-m telescope by re-imaging the fields on photometric nights and using differential photometry to produce the light curves. On all nights, as noted in Section 2.3.2, a large number of field stars were measured in the frames along with the comet. We computed the magnitudes of all the field stars using the Kron–Cousins filter system from Mauna Kea for all the field stars, even for photometric nights that had independent calibration, and then computed a magnitude correction for each frame to ensure that the magnitudes of the field stars matched the calibrated values, and that the offsets were applied to the comet light curves. This differential technique not only placed all the datasets on the same system, but served to correct for small extinction variations on photometric nights. We have found that this technique works well to recover data when cirrus is present with extinction up to 1 mag.

We present a selected set of light curves in Fig. 8. The data set for the rotation analysis is extremely large, and the data were prepared iteratively. It was only after generating light curves and trying to combine datasets from different observatories that we were

Table 3
Keck spectroscopic observations.

Date (UT)	Exposure (s)	Airmass	r (AU)	Δ (AU)	α ($^\circ$)	Seeing
2004 December 04	1200 \times 5	1.74–1.20	2.435	2.435	23.3	<1"
2005 January 06	1200 \times 6	1.42–1.05	2.241	1.850	35.6	variable
2005 June 08	1200 \times 9	1.74–1.06	1.531	0.781	36.5	1.03"

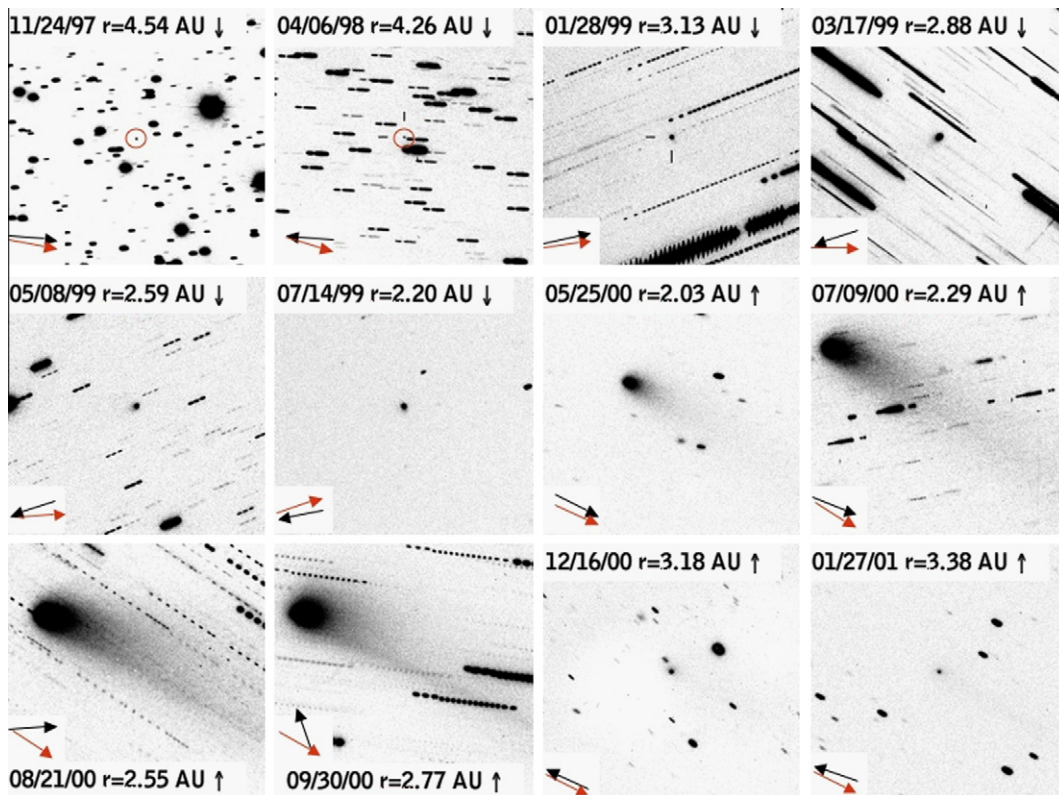


Fig. 4. See Table 4 for image details. Images are $3' \times 3'$. North is up East left in the images. The UT date and the heliocentric distance at the time of observation is noted at the top of each image. Pre-perihelion observations (inbound) are indicated with a downward arrow and post-perihelion observations with an upward arrow. The black and red arrows in the lower left of each image indicate the anti-solar direction and the negative of the comet's heliocentric velocity vector as seen in the plane of the sky. (For interpretation of the references to color in this figure legend, the reader is referred to the web version of this article.)

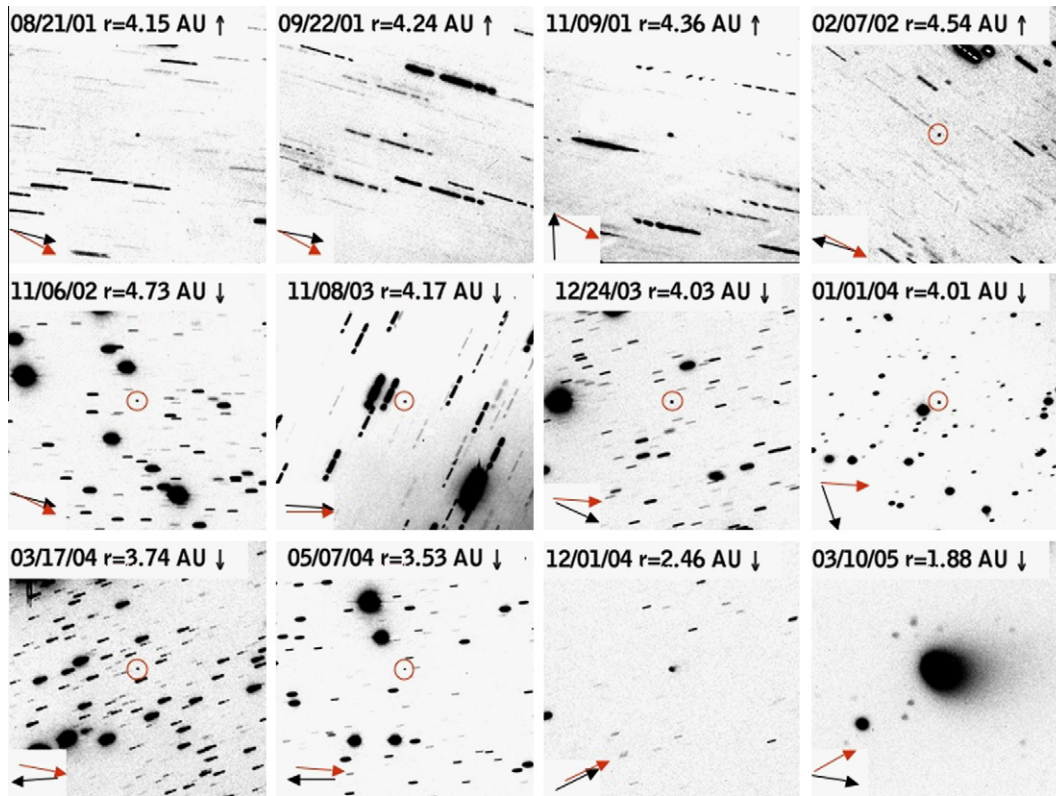


Fig. 5. See caption for Fig. 4.

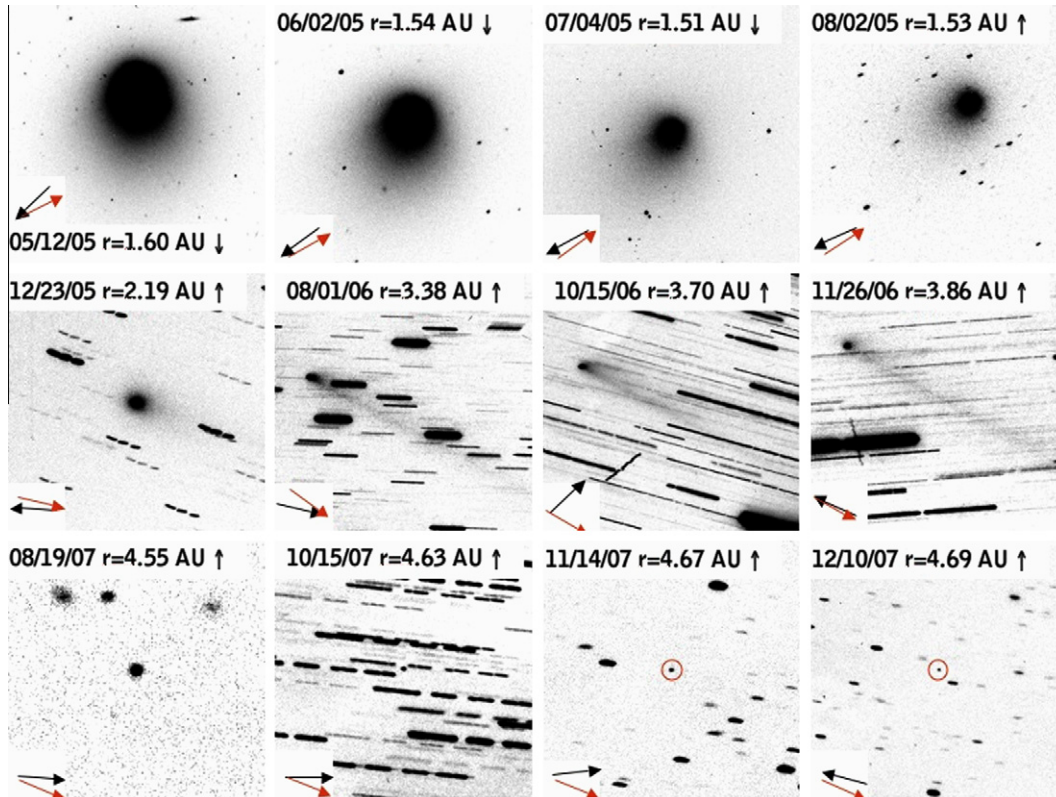


Fig. 6. See caption for Fig. 4.

alerted to problems in the data and could investigate further. This included developing techniques for background object and nebulosity subtraction, and ensuring that everything was placed on

the same photometric system. Some datasets required binning the photometry to increase the S/N (thus reducing the time resolution). The analysis of the rotation light curves is presented in paper

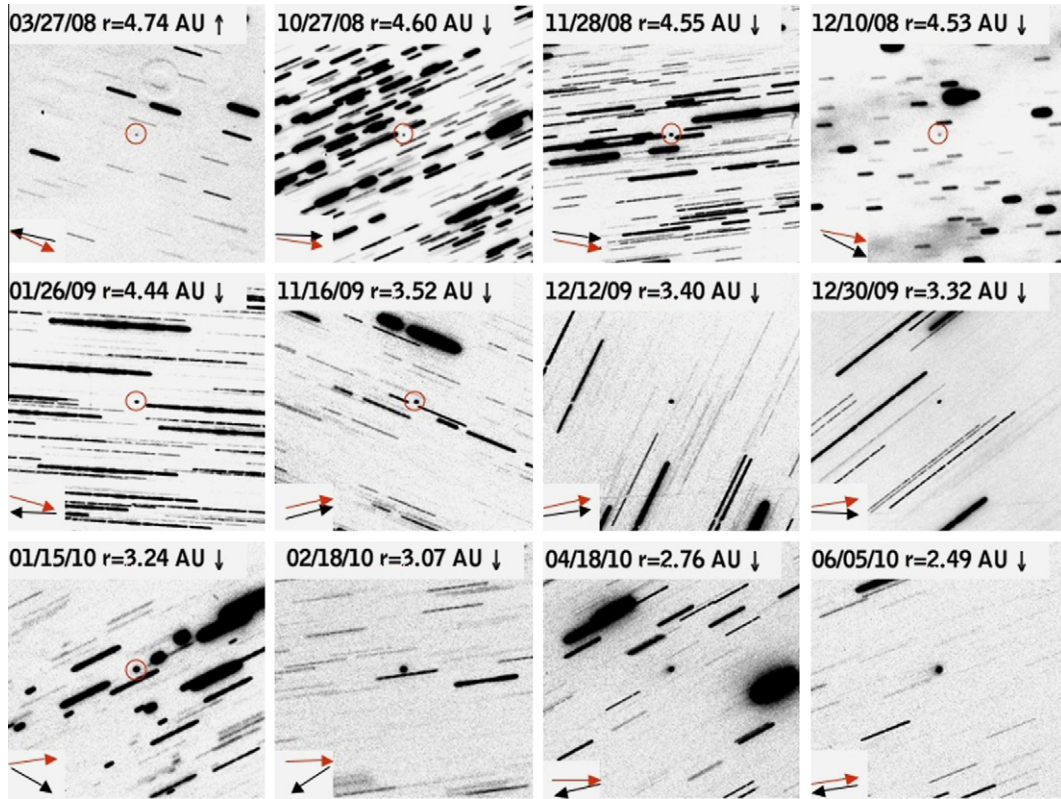


Fig. 7. See caption for Fig. 4.

II (Belton et al., 2011). However, from the figure it is clear that, with the long 1.7-day rotation period and maximum daily sampling at opposition of only 8 h at any particular observatory, having telescopes spread in longitude was key to removing sampling aliases.

2.3.4. The nucleus phase function

The photometric data beyond ~ 4.0 AU, where there was no apparent dust in the images, and it was expected that there was no activity, were corrected for observing geometry to unit heliocentric and geocentric distance ($R(1, 1, \alpha)$) via:

$$R(1, 1, \alpha) = m_R - 5.0 \log(r\Delta) \quad (1)$$

where m_R is the observed R magnitude, r is the heliocentric distance and Δ the geocentric distance in AU. An unweighted linear fit to the data produces a linear phase function of $\alpha = 0.045 \pm 0.001$ mag deg $^{-1}$ and a weighted fit gives $\alpha = 0.040 \pm 0.001$ mag deg $^{-1}$. The slight difference in slope is because the larger phase angle data have the biggest errors (fainter comet). We adopt the former value here. This is shown in Fig. 9.

Fig. 10 plots the reduced R magnitude, $R(1, 1, 0)$, where the linear phase coefficient, α has been removed:

$$R(1, 1, 0) = R(1, 1, \alpha) - 0.045\alpha \quad (2)$$

as a function of time. The reduced magnitude is plotted as a function of days from perihelion passage in Fig. 11 and as a function of heliocentric distance from perihelion in Fig. 12. Both figures show the asymmetry of the light curve about perihelion. In particular, the fading due to the drop in activity post-perihelion is much more gradual than the brightening was pre-perihelion.

2.3.5. Low-resolution spectroscopy

Before integrating the flux within emission bands, we removed both the sky background and the underlying continuum, the latter

resulting from reflected sunlight by dust. To remove the dust continuum, the spectrum of the solar-analog star SA 102-1081 was used for the 2005 January data and the spectrum of HD 120050 was used for the 2005 June data, which were obtained with the same setup on the nights the comet was observed. We took sky spectra that were free from the cometary contamination on 2004 December 04 and 2005 June 5, respectively. However, no sky was observed on 2005 January 6. Therefore, the sky background for January 6 was measured using the first and last 10 rows on the edges of the spectral image of the comet. This assumed that there are no cometary emissions at that distance from the optocenter. This assumption is certainly valid for C₂ and C₃; since they were still weak and did not extend too far during January 2005. However, in terms of stronger emission from CN, the amount of CN which might be reduced even in that part of the spectrum was visually noted to be minimal. The details of sky and solar subtraction are described in Cochran et al. (1992). Fig. 13 shows the spectra from all three nights.

After removing the solar spectrum, the comet spectra consisted only of gas fluorescence emission features. The fluxes in the gas bandpasses were summed up to determine the integrated band flux. The bandpasses used are listed in Table I of Cochran et al. (1992). The integrated fluxes were then converted to column densities using the constants in Table II of Cochran et al. (1992). The Swings effect was taken into account for the CN, NH and OH.

In turn, a simple Haser model (Haser, 1957) was used to convert the column densities to gas production rates with two important parameters: (1) the number of photons scattered per second per radical (the so-called emission rate factor g); and (2) the lifetime of the molecule, or the Haser scale length. The g -factors of CN, C₂, C₃, NH and OH are described in A'Hearn et al. (1995). We have adopted the outflow velocity of 0.85 km s $^{-1}$ at 1 AU for 9P/Tempel 1 from Cochran et al. (2009). The scale lengths used are listed in Table 5.

Table 4
Details of composite images.

UT Date mm/ dd/yy	r^a (AU)	I/ O ^b	$T-q^c$ (dys)	Af ρ (cm)	Exp ^d (s)	Scale ^e ($\times 10^5$ km)
11/24/97	4.54	I	-769	13.95	600	4.76
04/06/98	4.26	I	-636	9.19	2200	5.98
01/28/99	3.13	I	-339	31.88	8200	2.83
03/17/99	2.88	I	-291	10.08	12300	2.95
05/08/99	2.59	I	-239	27.26	900	3.49
07/14/99	2.20	I	-172	85.43	180	3.84
05/25/00	2.03	O	+144	156.18	300	2.74
07/09/00	2.29	O	+189	132.45	3600	2.42
08/21/00	2.55	O	+232	138.99	7800	2.18
09/30/00	2.77	O	+272	134.97	4800	2.36
12/18/00	3.19	O	+351	37.05	300	4.03
01/27/01	3.38	O	+391	30.08	450	5.00
08/22/01	4.15	O	+598	8.88	9900	5.12
09/22/01	4.24	O	+629	10.98	12600	4.65
11/09/01	4.36	O	+677	21.83	23850	4.40
02/07/02	4.54	O	+767	9.92	5400	5.98
11/06/02	4.73	I	-972	15.16	3600	5.05
11/08/03	4.17	I	-605	12.11	6600	4.74
12/24/03	4.03	I	-559	20.03	900	4.01
01/01/04	4.01	I	-551	19.94	300	3.96
03/17/04	3.74	I	-475	7.24	2600	4.56
05/07/04	3.53	I	-424	9.67	2400	5.25
12/01/04	2.45	I	-216	27.81	400	3.25
03/10/05	1.88	I	-117	236.10	340	1.27
05/12/05	1.60	I	-54	330.81	100	0.94
06/02/05	1.54	I	-33	433.57	100	0.99
07/04/05	1.51	I	-1	482.77	100	1.16
08/02/05	1.53	O	+28	492.05	120	1.41
12/23/05	2.19	O	+171	216.42	900	3.64
08/01/06	3.38	O	+392	22.81	7800	4.11
10/15/06	3.70	O	+467	35.92	26100	3.55
11/26/06	3.86	O	+509	27.61	20700	4.03
08/19/07	4.55	O	+775	13.35	133	6.01
10/15/07	4.63	O	+832	9.64	16000	5.04
11/14/07	4.67	O	+862	17.56	100	4.82
12/10/07	4.53	O	+888	11.40	900	4.65
03/27/08	4.74	O	+996	9.00	2700	6.93
10/27/08	4.60	I	-807	10.30	9900	5.21
11/28/08	4.55	I	-775	15.27	20700	4.73
12/10/08	4.53	I	-763	17.74	13200	4.65
01/26/09	4.44	I	-716	12.70	21600	4.87
11/16/09	3.52	I	-416	10.19	12600	4.13
12/12/09	3.40	I	-422	15.37	16500	3.52
12/30/09	3.32	I	-378	20.69	24000	3.19
01/15/10	3.24	I	-362	26.58	3600	2.99
02/18/10	3.07	I	-328	25.72	5400	2.87
04/18/10	2.76	I	-269	19.82	4050	3.38
06/05/10	2.48	I	-221	28.28	2400	3.81

^a Comet heliocentric distance.

^b I = Inbound leg of orbit (pre-perihelion); O = Outbound leg of orbit (post-perihelion).

^c Number of days pre- or post-perihelion.

^d Total effective exposure time for the composite image.

^e Scale of the image in km per side.

2.3.6. Dust dynamical modeling

The Finson–Probstein (FP) technique is a dust-dynamical model originally developed by [Finson and Probstein \(1968\)](#) which can be used to track the trajectories of dust grains leaving a comet nucleus after they decouple from the gas flow and are influenced only by solar radiation pressure and solar gravity. With this technique, surface brightness data of comet dust tails can be inverted and information about the grain size distribution, ejection velocity, and onset and cessation of activity can be obtained. We employ this technique for the data around the 2000 perihelion passage to help understand the activity and dust properties.

Once dragged from the nucleus in the gas flow, the dust is decoupled from the flow within a few nuclear radii. The motion of the dust grains is then controlled by solar gravity and solar radi-

ation pressure, both acting approximately radially, in opposite directions. The net result of the two influences is a reduced gravitational force acting upon the dust. The parameter β is defined as the ratio of the radiation pressure force to the gravitational force. For grains of radius a (m) and density, ρ (kg m^{-3}), β is given by:

$$\beta = 5.740 \times 10^{-4} \frac{Q_{pr}}{\rho a} \quad (3)$$

where Q_{pr} is the radiation pressure efficiency (typically 1–2, dependent on the material scattering properties). The FP method involves computing the trajectories of dust grains ejected from the nucleus at velocity v and under the influence of solar gravity and radiation pressure. The scattered light from a distribution of dust emitted from the nucleus over a range of times as they move away from the comet is computed and then compared to the surface brightness of the imaged dust.

Five Comet 9P/Tempel 1 datasets were modeled: March 19, 1999 (pre-perihelion), May 26, July 9, August 21, and September 30, 2000 (post-perihelion) using a pseudo Finson–Probstein code ([Farnham, 1996](#)). All the images were median combined, and in general this worked well to obtain star-free images of the low surface brightness dust tail (see [Fig. 14](#)). Because the dust in the tail followed a trajectory expected for emission from a point source, the models did not include emission relative to the comet's rotation axis. The best models did include greater emission from the sunward direction (see [Fig. 15](#) for the emission function), which agrees with spacecraft encounter emission data which show maximum outgassing at the subsolar point. This is indicative of a very low thermal conductivity for the surface materials ([A'Hearn et al., 2005](#)). [Fig. 15](#) compares the result of the FP modeling to the imaging data from August 21, 2000.

Four models corresponding to 144, 188, 230, and 271 days post-perihelion, produced similar model parameters (see [Table 6](#)). These showed that particle emission began 200 days before perihelion ($r = 2.9$ AU), and continued until the date of observation. The data were best fit with particle sizes ranging from $3 \mu\text{m}$ to $1000 \mu\text{m}$, with emission rates proportional to a^{-1} . All four dates used similar particle velocities, with smaller particles having larger velocities. The particle velocities were adjusted during the modeling process, but varied on a roughly logarithmic scale with size, with velocities for each set of observations being identical except for a small variance in velocities of the larger particles ($100 \mu\text{m}$ and greater). The velocities for the smaller particles, ranging from sizes 3 to $300 \mu\text{m}$, were $9\text{--}16 \text{ m s}^{-1}$ for all data. The modeling is much more sensitive to small variations in particle size rather than their velocities, and identical particle velocities for all the dates would still give good results. It should also be noted that particles smaller than $30 \mu\text{m}$ emitted before perihelion did not show up in the models; these small particles have moved so far from the nucleus that they have left the image by the time the comet was observed. This implies that activity may have occurred well before 200 days prior to perihelion ($r = 2.9$ AU), but that this activity consisted of small particles and we have no information about this from these images.

The four post-perihelion observations also gave similar particle production rates, with each date having identical relative production rates, with the absolute rates varying at most by less than an order of magnitude (see [Table 6](#)). The rates peaked at perihelion and remained stable for 100 days afterward, with a fall off at times before and after. Determining the production rates is the last step in the modeling process, since they do not influence the contours of the model. The contours are dependent on flux, and flux scales linearly with production rate. In general, other parameters were adjusted to get the contours of the model to agree with the data, and then the particle production rate was adjusted (see [Fig. 15](#)).

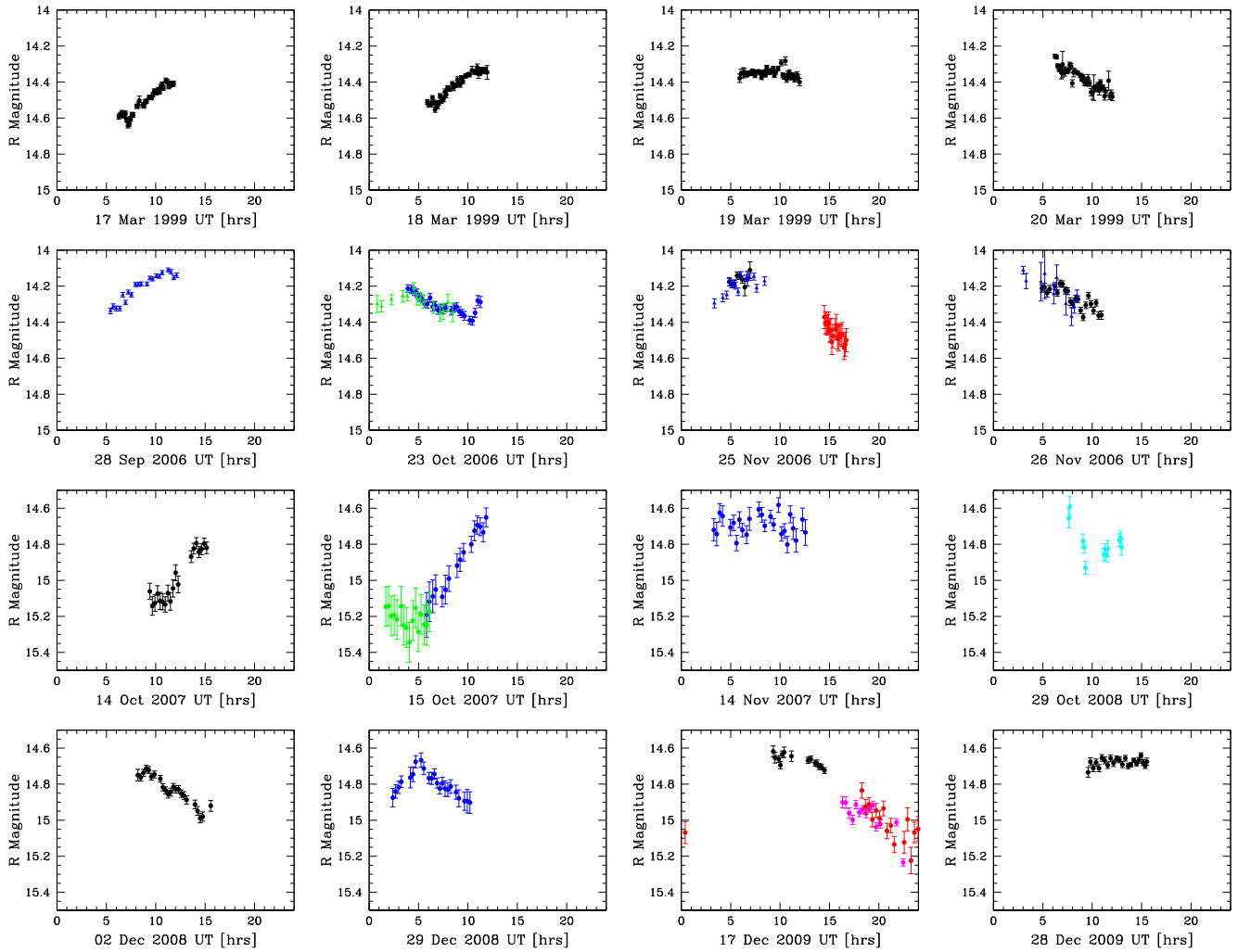


Fig. 8. Representative Comet 9P/Tempel 1 light curves. Reduced R-band magnitude is plotted versus UT for a selection of dates. The value of having observatories at different longitudes is evident for several of the dates, and was especially important to help remove the diurnal sampling aliases for this slowly rotating comet. Color Key: Black – Mauna Kea, cyan – Palomar, blue – Lowell, Kitt Peak (triangles), red – India, magenta – China, green – La Palma, ESO (triangles). (For interpretation of the references to color in this figure legend, the reader is referred to the web version of this article.)

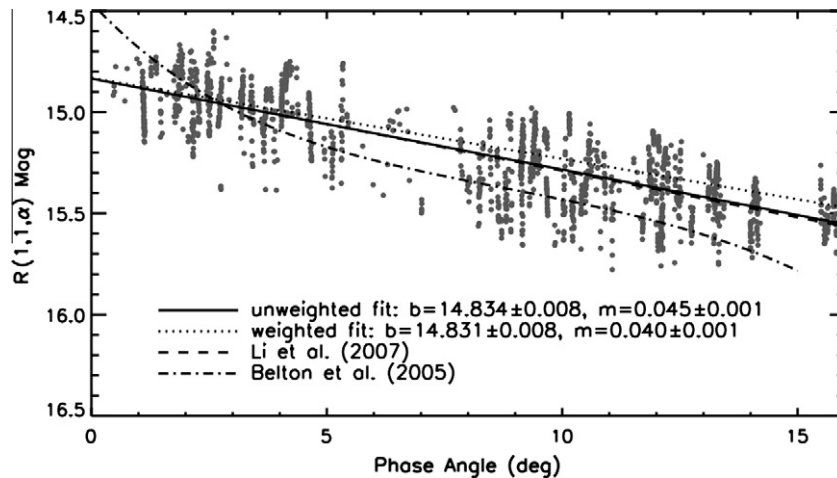


Fig. 9. The $R(1,1,\alpha)$ data are plotted versus phase angle for Comet 9P/Tempel 1. The dotted line represents an unweighted linear fit to the data and the solid line is a weighted fit. Data at small phase angles dominate the weighted fit. The dashed line represents the fit from resolved encounter images (Li et al., 2007) and agrees well with the data. The fit from Belton et al. (2005) used a much smaller set of ground-based measurements.

The production rate adjustments were determined by subtracting the model from the data and assessing at the residuals. On the

whole, the 2000 9P/Tempel 1 data displayed remarkably similar modeling parameters. The particle sizes, emission times, velocities,

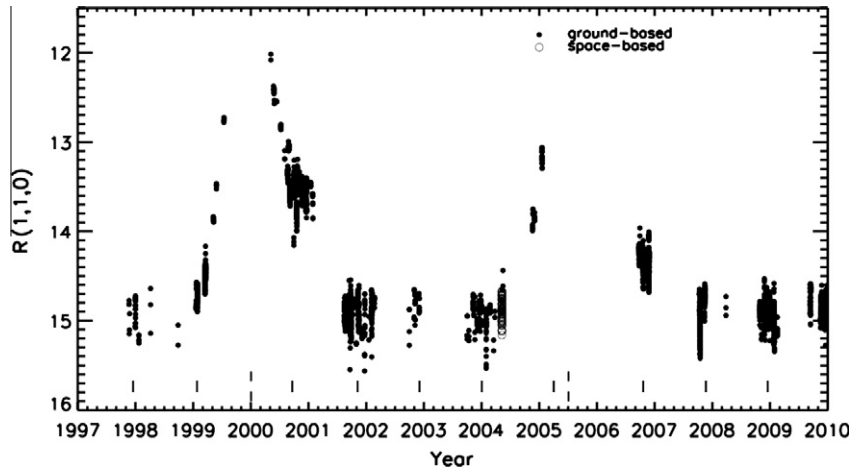


Fig. 10. $R(1,1,0)$ versus calendar year. The data have been corrected to zero phase angle using a linear phase law of $0.045 \text{ mag deg}^{-1}$. The flat trend between 2001 and 2004 indicates that coma there is negligible and the scatter in that region is almost entirely due to the spin of the nucleus. The open circles are the HST data of Lamy et al. (2007).

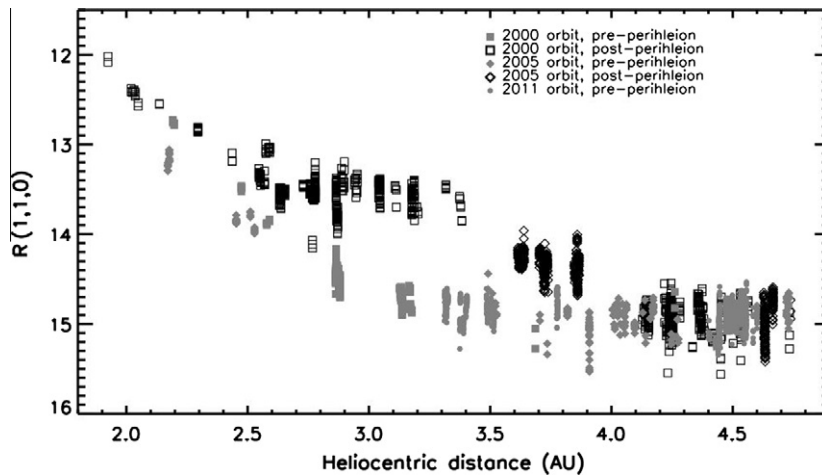


Fig. 11. $R(1,1,0)$ versus heliocentric distance. The brightness asymmetry about perihelion is clearly evident. Notice that the mean trend becomes independent of heliocentric distance beyond 4 AU, which indicates that light scattered from the nucleus dominates the signal.

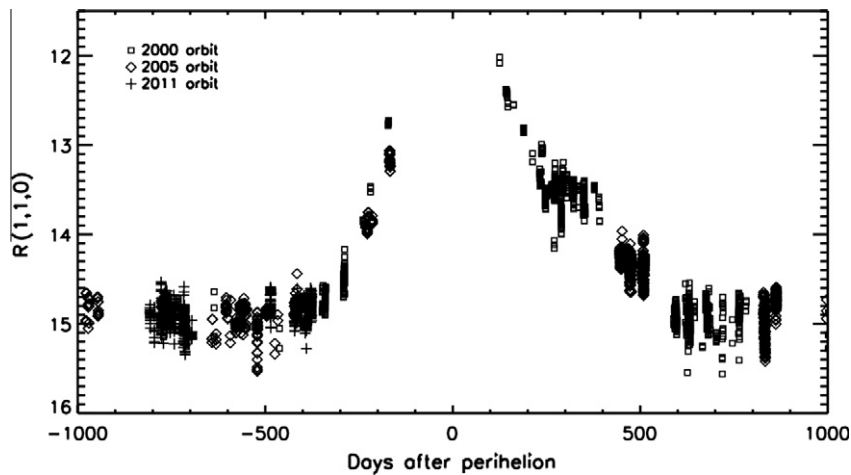


Fig. 12. $R(1,1,0)$ versus time from perihelion passage. This figure shows the repeatability of the data from one perihelion to the next and also the asymmetry of the light curve about perihelion.

production rates, and emission functions were all within an order of magnitude of each other (and in most cases identical).

An additional model was made for March 19, 1999, corresponding to 289 days before perihelion. This model displayed some sim-

ilar characteristics to the post-perihelion models, but also some differences (see Table 6). Although the particle production rates are much higher before perihelion, there is still consistency in the models if one notices particle size. The particles emitted before

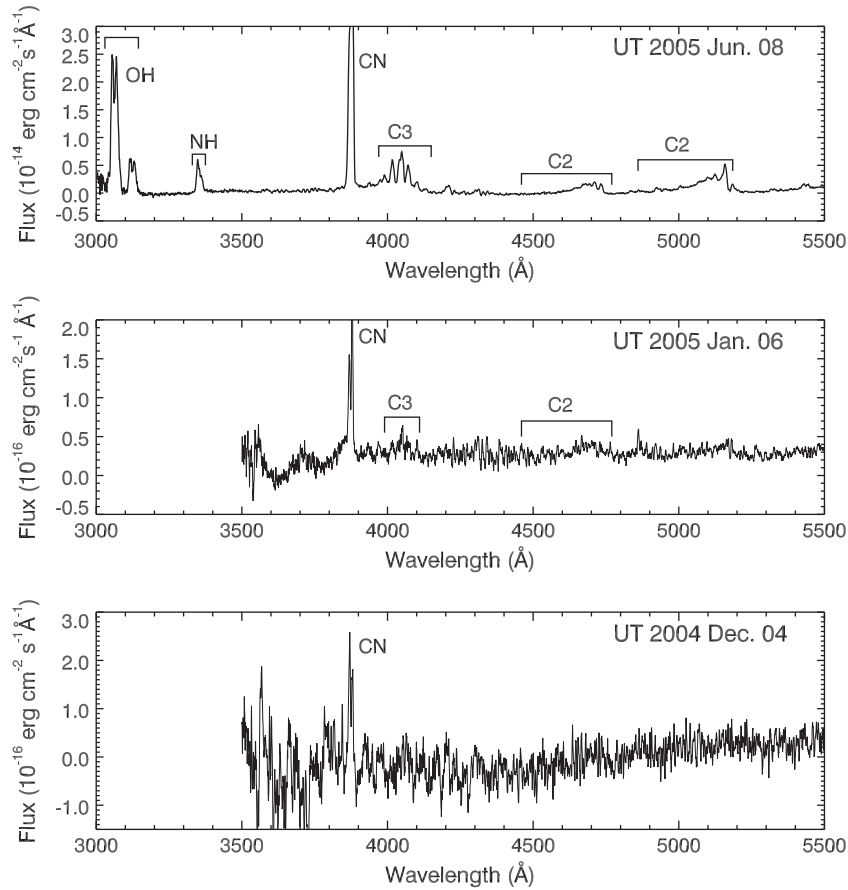


Fig. 13. Spectra of Comet 9P/Tempel 1 obtained with LRIS on the Keck I telescope showing the development of the gas emission. The heliocentric distances and days before perihelion, q , for the spectra are (top to bottom): June 8, 2005 ($r = 1.531$ AU; $q = 27$ dy), January 6, 2005 ($r = 2.241$ AU; $q = 180$ dy), December 4, 2004 ($r = 2.435$ AU; $q = 212$ dy).

perihelion were small and would not be observed after perihelion because their speed carried them far from the nucleus. These particles would not be included in the rates from models after perihelion. Additionally, large particles reflect more light and contribute more to flux than smaller particles, so a higher production of small particles is needed to account for the observed flux prior to perihelion. Another difference not shown in the table is that the relative emission rate of particles was proportional to a^{-3} in the pre-perihelion model, as opposed to a^{-1} in the post-perihelion models. It should be noted that the dust onset, or activity “turn-on” determined from the pre-perihelion data is a limit, *i.e.* that activity had begun by $q = 350$ days ($r = 3.2$ AU), although it could have begun much earlier, but we do not have the information in the images for small grains.

2.3.7. Monte-Carlo dust modeling

Based on the Monte-Carlo dust modeling (Samarasinha et al., 2004), Comet 9P/Tempel 1’s persistent southern dust feature ob-

served in visible wavelengths during early 2005 is compatible with low dust velocities (~ 20 m s^{-1}) (Vasundhara, 2009). The appreciable curvature of this dust feature indicates that radiation pressure effects are significant. Modeling suggests that the radiation pressure parameter, β , is of the order of 0.1 and that β increases at larger cometo-centric distances. The low dust velocities are suggestive of large dust grains (\sim several microns) whereas the relatively large β values (for that grain size) indicate that these grains may have larger cross sectional areas than the canonically accepted values. This scenario is consistent with large fluffy dust grains (Samarasinha et al., 2004). Furthermore, indications for increasing β with increasing cometo-centric distance are suggestive of fragmentation of these large dust grains as they move away from the nucleus. Fig. 16 shows the Monte-Carlo simulation for the persistent southern dust feature seen during spring 2005. The simulation assumes an initial dust ejection velocity of 20 m s^{-1} and a constant β of 0.1. The rotation pole of Thomas et al. (2007) is adopted in the simulations.

2.4. Onset and cessation of activity – water-sublimation models

We used a simple sublimation model (Meech et al., 1986) to evaluate the comet’s activity as a function of distance, r from the Sun. Once there is sufficient energy for ices to sublimate, the gas mass loss may be obtained from the energy balance equation for a nucleus in thermal equilibrium (neglecting conduction in this approximation):

$$\frac{F_{\odot}(1-A)}{r^2} = \chi \left[\epsilon \sigma T^4 + L(T) \frac{dm_s}{dt} \right] \quad (4)$$

Table 5

1 AU Haser model scale lengths.

Molecule	Parent scale length (km)	Daughter scale length (km)
CN ^a	1.7×10^4	3.0×10^5
C ₃ ^a	3.1×10^4	1.5×10^5
C ₂ ^a	2.5×10^4	1.2×10^5
NH ^b	5.0×10^4	1.5×10^5
OH ^c	2.4×10^4	1.6×10^5

^a Determined from Cochran et al. (1992).

^b Determined from Randall et al. (1992).

^c From Cochran and Schleicher (1993).

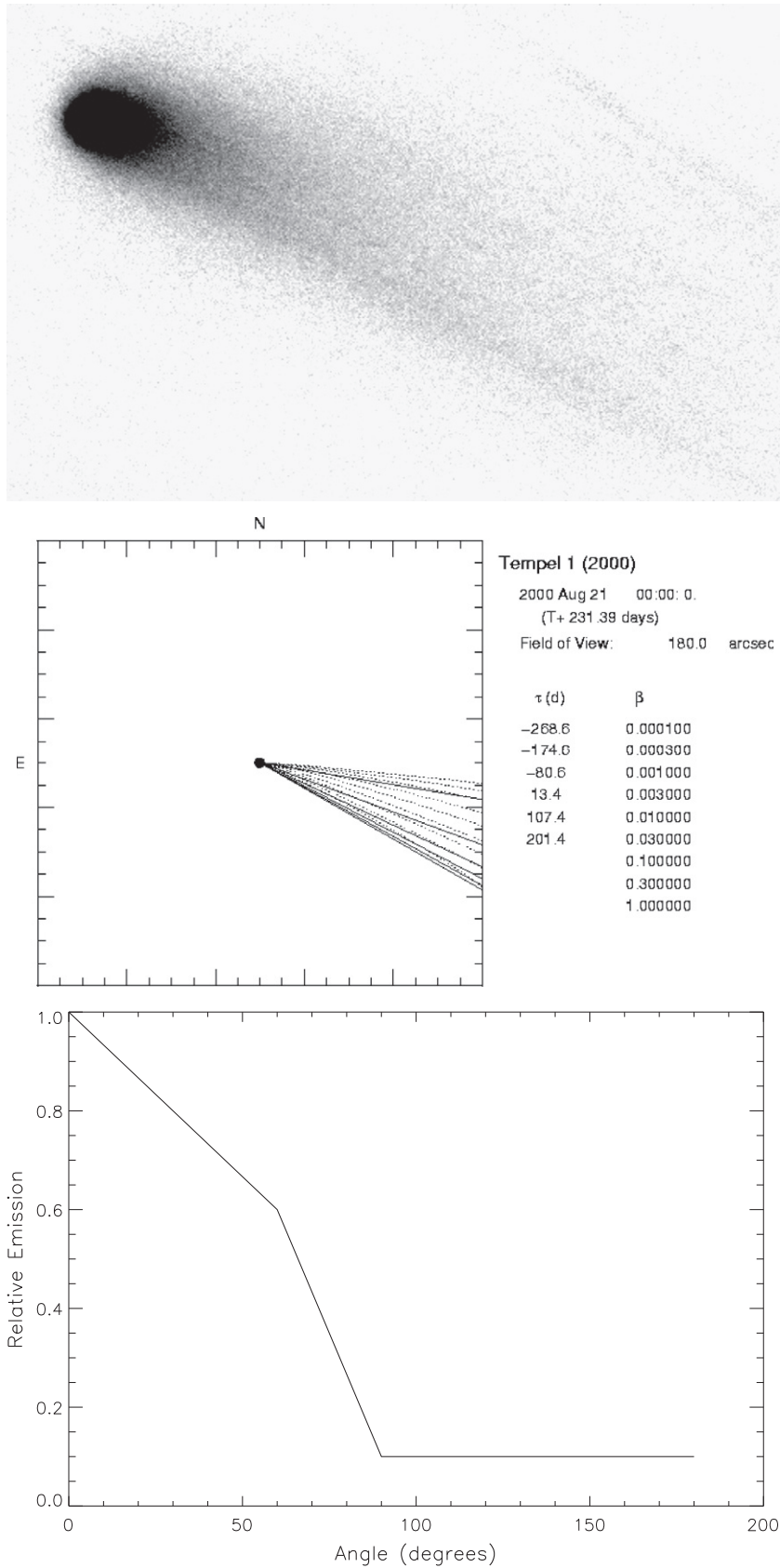


Fig. 14. (a) Median combined composite image of Comet 9P/Tempel 1 from August 21, 2000. North is up and East is to the left. This image is 2.65 by 1.70×10^5 km in the plane of the sky. (b) Plot showing the expected dust particle trajectories (syndynes and synchrones) for the same date. τ is days relative to perihelion and β (the particle size parameter) corresponds to a $0.3 \mu\text{m}$ radius dust grains. (c) Dust mission function for all models between 1999 March and 2000 September. Zero degrees corresponds to the sunward direction.

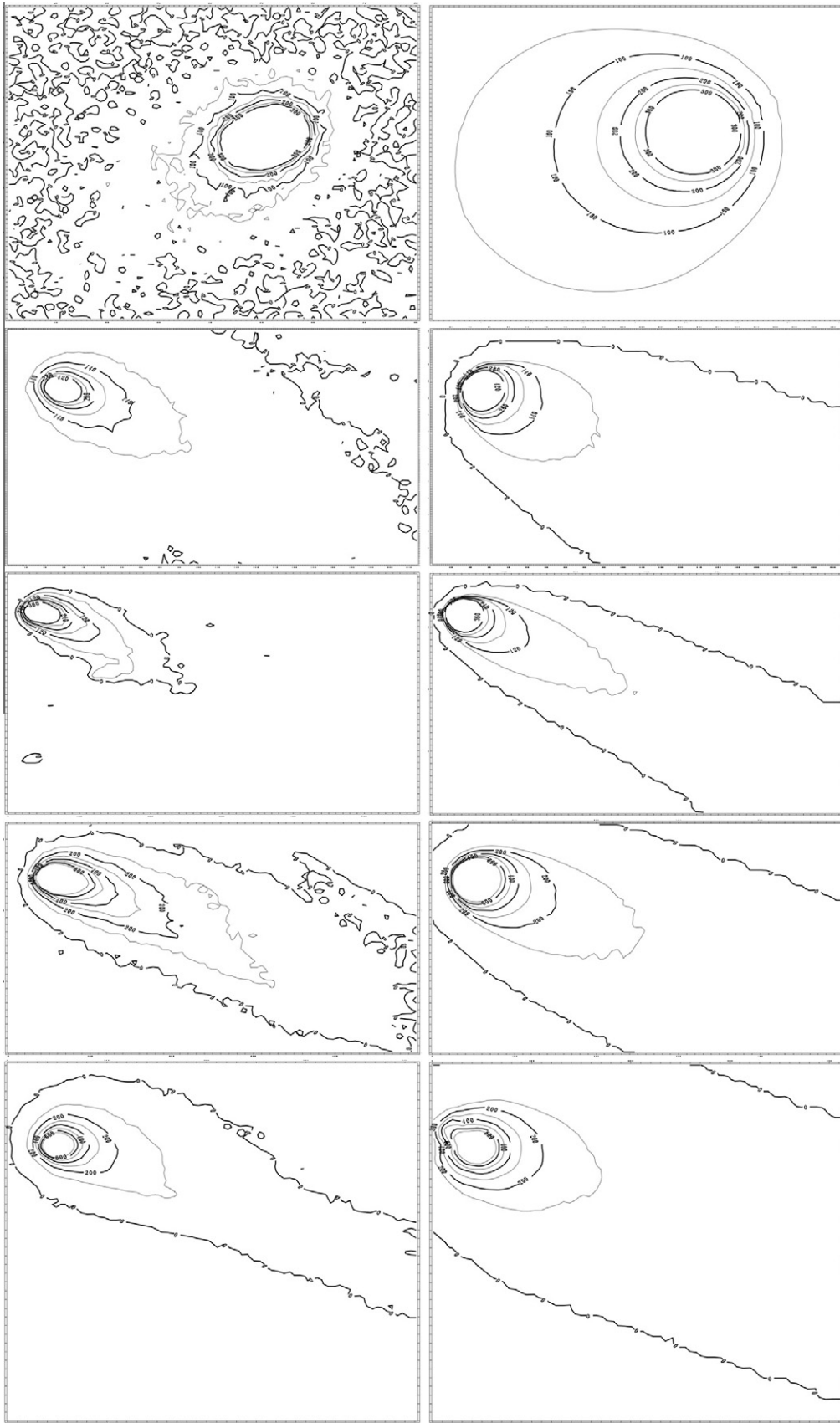


Fig. 15. Contour plots of Comet 9P/Tempel 1 data for the median combined composites (left side) and for the best fit FP dust-dynamical models on the right. The rows from top to bottom correspond to the dates: March 19, 1999 (pre-perihelion), May 26, July 9, August 21 and September 30, 2000 (post-perihelion). North is up and East is to the left.

where F_{\odot} is the solar constant, A is the albedo, χ takes account of the rotation (a slow rotator has $\chi=2$ and an isothermal nucleus has $\chi=4$), ε is the infrared emissivity and σ is the Stephan–Boltzman constant. The latent heat as a function of temperature, $L(T)$ (J kg^{-1}) is fit to data (Cowan and A'Hearn, 1982), and the mass loss rate per unit area, dm_s/dt is related to the sublimation vapor pressure $P(T)$ via

$$\frac{dm_s}{dt} = P(T) \left[\frac{\mu m_H}{2\pi kT} \right]^{1/2} \quad (5)$$

where $(2kT/\mu m_H)^{1/2}$ is the thermal gas velocity. These equations are solved iteratively for the mass loss. The escaping gas will drag dust from the surface layers, and assuming a dust to gas mass ratio and a particle size distribution, this can be used to calculate the amount of scattered light from dust in the coma. The total mass of grains in the observing aperture is equal to the mass loss from the nucleus, dM/dt (kg s^{-1}) times the time, t , spent in the diaphragm

$$(p_v \beta^2)_{coma} = \left[\frac{3p_v}{4\pi\rho a} \frac{dM}{dt} \right] t \quad (6)$$

where $(p_v \beta^2)_{coma}$ is the grain cross section (m^2), p_v the geometric albedo, ρ the grain density (kg m^{-3}) and a (m) the grain radius. The coma grain cross section is related to the total coma brightness via:

$$(p_v \beta^2)_{coma} = 2.24 \times 10^{22} r^2 \Delta^2 10^{0.4(m_{\odot} - m_{coma})} 10^{\beta_p \alpha} \quad (7)$$

where m_{\odot} is the solar magnitude and m_{coma} the brightness of the coma dust, and r and Δ are the heliocentric and geocentric distances in AU. The product $\beta_p \alpha$ is the phase correction, where β_p is the phase function (see Section 2.3.4) and α ($^{\circ}$) is the observed phase angle.

The coma flux is then added to that from the nucleus for comparison with the observed heliocentric light curve.

The fixed parameters used for the fits are shown in the left column of Table 7. Because so much is known about the nucleus from the encounter and ground-based observations, for this simple model the main free parameters are effectively the outgassing rate and the grain sizes. However, these are coupled because what we are really measuring with the photometry is the scattering cross sectional area, which is a product of the number of grains times the cross sectional area per grain. To look at first order effects, we therefore used only a single particle size ($a = 1 \mu\text{m}$). It was not possible to fit the light curve with a single fractional active area on the nucleus, this changed with heliocentric distance. Thus, a series of models were run to systematically change the active area both inbound and outbound and these parameters are shown in the right hand column of Table 7. The model fits compared to the data are shown in Fig. 17. The model outputs in addition to the predicted total coma brightness, the dust production rate as a function of distance, the surface ice temperature, and the critical dust size, a_{crit} , the maximum size that can be lifted from the nucleus

$$a_{crit} = \frac{9\mu m_H Q v_{th}}{64\pi^2 \rho_{dust} \rho_{nuc} R_N^3 G} \quad (8)$$

where Q (mol s^{-1}) is the gas production rate, ρ_{dust} and ρ_{nuc} (kg m^{-3}) are the dust and nucleus densities, respectively, R_N (m) is the nucleus radius and G the gravitational constant. At the point at which activity caused a noticeable brightening in the 9P/Tempel 1 light curve, $a_{crit} \sim 3 \mu\text{m}$.

Table 6
Parameters for Finson–Probstein model of Comet 9P/Tempel 1.

Image (date)	Dust onset ^a (dy)	Obs. ^a (dy)	a_{min}^b (μm)	a_{max}^b (μm)	F_{min}^c (s^{-1})	F_{max}^c (s^{-1})	v_{gr}^d (m s^{-1})
3/19/99	–350	–289	3	30	3.5×10^{13}	5.0×10^{13}	n/a
5/26/00	–200	144	3	1000	4.2×10^8	5.4×10^8	2.2–5.0
7/09/00	–200	188	3	1000	1.4×10^8	1.8×10^8	2.2–5.0
8/21/00	–200	230	3	1000	2.52×10^8	3.78×10^8	2.16–6.0
9/30/00	–200	271	3	1000	1.8×10^8	2.9×10^8	2.4–6.0

^a Days with respect to perihelion, (–) pre- and (+) post. Dust onset is the modeled activity initiation, Obs. is the date of the observed image from which the dust onset was modeled.

^b Min and max grain size used in fit.

^c Min and max particle flux.

^d Grain velocities for sizes 1000–300 μm . Other model parameters are not listed for each model because they do not change. For instance, the velocities of particles less than 300 μm were identical for all five apparitions.

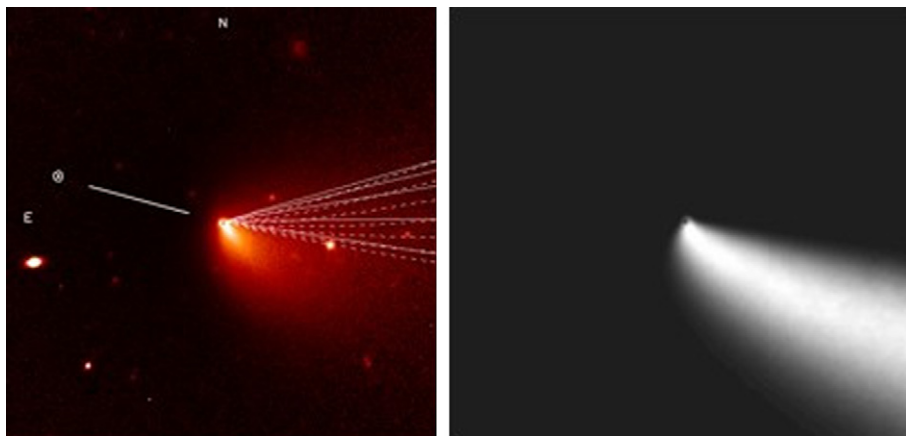


Fig. 16. On the left, a persistent southern dust feature (observed on March 12, 2005 in R-band). The projected solar direction, as well as the synchronones (solid lines) and syndynes (dashed lines) are marked; North is up and East to the left in the images, and the scale is 7.8×10^4 km projected in the plane of the sky. On the right is a simulation of the observations. Both the observation as well as the simulation were enhanced by division by an $1/\rho$ profile, where ρ is the sky-plane projected cometo-centric distance.

Table 7
Water-sublimation model parameters.

Fixed parameter	Value	Reference	Model region	$f_{\text{active}} \text{ '00}^{\text{a}}$	$f_{\text{active}} \text{ '05}^{\text{a}}$
Ice type	H ₂ O		Inbound: Q to 3.25 AU	0.0007	0.0007
Albedo	0.039	Li et al. (2007)	Inbound: 3.25–2.8 AU	0.0014	0.0014
Emissivity	0.9	Groussin et al. (2007)	Inbound: 2.8–2.4 AU	0.0018	0.0017
Phase coeff. (mag deg ⁻¹)	0.045	This paper	Inbound: 2.4–2.2 AU	0.0045	0.0035
Grain density (kg m ⁻³)	10 ³	Assumed	Inbound: 1.9 AU to q		0.01
Grain size (m)	10 ⁻⁶	Assumed	Outbound: 2.0–2.6 AU	0.005	
Grain size distn.	No		Outbound: 2.6–3.2 AU	0.006	
Nucleus radius (m)	3000	A'Hearn et al. (2005)	Outbound: 3.2–3.4 AU	0.007	
Rotation rate	Slow	Belton et al. (2011)	Outbound: 3.4 AU to Q	0.0085	

Note. The parameters which were held fixed for all the models are shown on the left of the table; the right side has the fit parameters as a function of apparition.

^a Free parameter for model fits: fractional nucleus surface area.

3. Discussion

3.1. The nucleus phase function

The preliminary analysis of the disk integrated phase function of the nucleus of Comet 9P/Tempel 1 allows us to determine the linear portion of the phase curve: $\beta = 0.045 \pm 0.001 \text{ mag deg}^{-1}$ ((see Fig. 9), in agreement with the analysis of the *in situ* disk-resolved images from the spacecraft (Li et al., 2007)). This value falls well inside the range known from other cometary nuclei (0.025–

0.083 mag deg⁻¹) and measured over a similar phase angle range, and it is close to the mean value of the sample distribution (0.053 mag deg⁻¹ out of 16 published linear phase function slopes of 12 cometary nuclei). The linear portion of the curve is controlled by surface roughness (in particular at large phase angles), and there is a correlation between the geometric albedo and the linear phase coefficient. The optical geometric albedo of the nucleus is $p_V = 0.056 \pm 0.007$ (Li et al., 2007).

In contrast to an earlier analysis (Belton et al., 2005), there is no evidence at this stage for any non-linear increase in brightness (e.g. an opposition surge) at small phase angles (below 2°). The magnitude and shape of an opposition effect are caused by the porosity of the surface materials and the albedo. Within the large dataset, we had three periods where the observing geometry afforded us the opportunity to observe at small phase angles: August–November 2001, $r = 4.3 \text{ AU}$ outbound, $14.1 < \alpha \text{ (}^\circ\text{)} < 1.2$; October–December 2003, $r = 4.3 \text{ AU}$ inbound, $13.4 < \alpha \text{ (}^\circ\text{)} < 1.8$; and August–November 2007, $r = 4.6 \text{ AU}$ outbound, $12.7 < \alpha \text{ (}^\circ\text{)} < 0.5$. For the 2007 period, we obtained a series of high S/N observations using the Gemini 8-m telescope. Now that we understand the rotation to a high level of accuracy, in a subsequent paper we will remove the rotation signature for these data sets to search for non-linear phase effects at small phase angles.

3.2. Onset of gas production and activity

As was shown in Meech et al. (1986) sublimation of surface or near-surface water ice can begin to lift micron-sized dust from the surface of a comet as far out as $r \sim 5\text{--}6 \text{ AU}$ from the Sun. Perhaps the most important indicator of activity in a comet is an excess in brightness seen when plotting the heliocentric light curve from which the geometric variation has been removed (see Fig. 17). Another indication is the appearance of a dust coma, but typically this is not noted until significant amounts of dust are present. This is because of two factors. First, small amounts of dust will have very low surface brightness and not be detectable against the background sky except in very deep exposures. Secondly, the dust may not be resolvable beyond the image PSF at large distances. Finally, direct spectroscopic observation of gas can be made.

The shape of the 9P/Tempel 1 light curve at the time that activity begins is consistent with the behavior of water-ice sublimation and does not require any more volatile species, such as CO or CO₂. The more volatile species, if present, are likely to be at greater depth in the nucleus, having been removed from the near-surface layers in the previous perihelion passage. Inbound, the deeper layers are still very cold from aphelion as the heat starts to penetrate the surface and the heat first reaches less volatile materials closer to the surface.

As shown in Table 7 the models were consistent with an increase in the fractional active area up to perihelion, with the peak

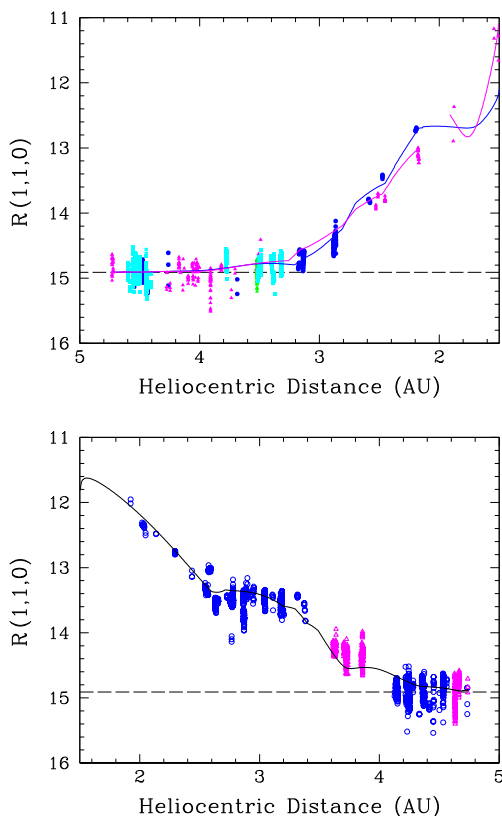


Fig. 17. Water-sublimation model for 9P/Tempel 1 plotted over multi-apperition datasets (blue: 2000 apparition; magenta: 2005 apparition, cyan: 2011 apparition) corrected to unit heliocentric and geocentric distance and zero degrees phase angle. The dashed line represents the rotationally averaged brightness of the nucleus. [Top] Pre-perihelion light curves. Blue solid curve uses parameters that fit the data from the 2000 apparition and the magenta curve fits the data from the 2005 apparition. [Bottom] Post-perihelion light curve. The solid line represents the fit that matches all data. The onset of sublimation with observable change in the comet brightness and dust production is around $r \sim 4.0 \text{ AU}$ and the turn off date is near $r \sim 4.6 \text{ AU}$. (For interpretation of the references to color in this figure legend, the reader is referred to the web version of this article.)

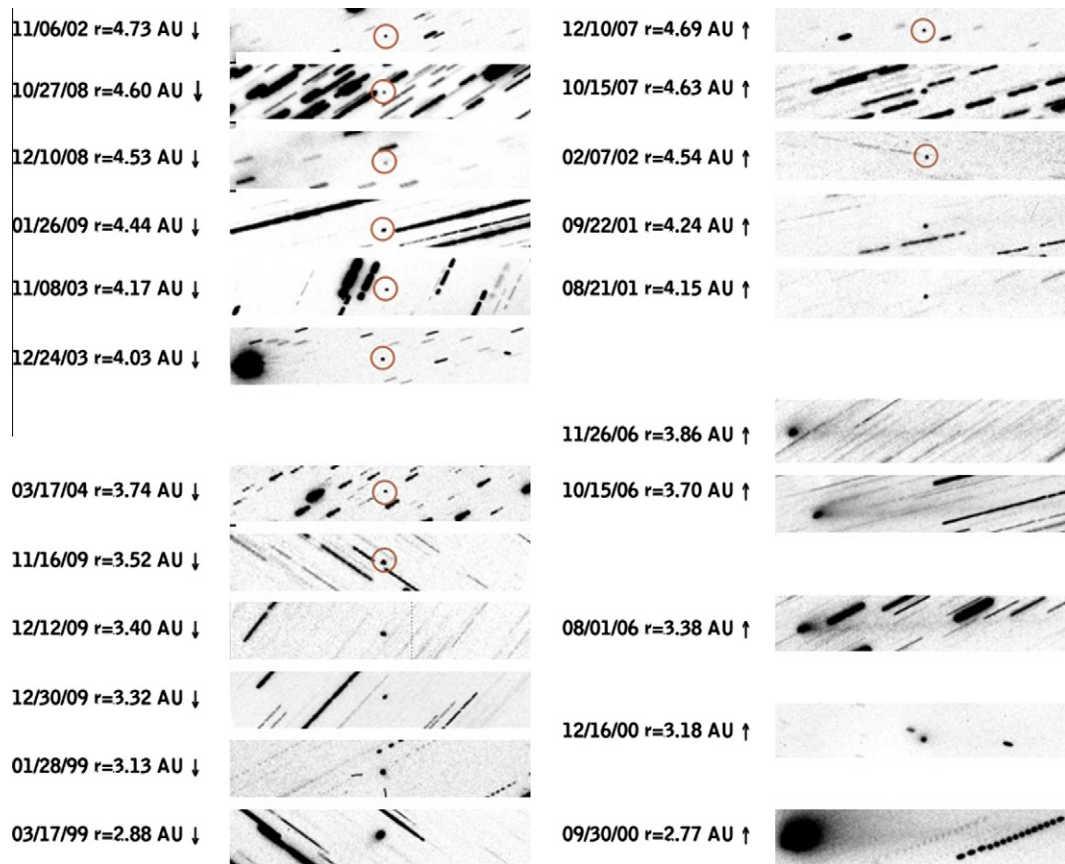


Fig. 18. Montage of Comet 9P/Tempel 1 images from aphelion ($r \sim 4.7$ AU) to $r = 2.7$ AU, covering the range of distances at which observable comet activity begins and ends. Dust and water models suggest that the activity begins near $r \sim 4$ AU, and ends near $r \sim 4.6$ AU. All of the images are about $180 \times 36''$, and have been rotated so that the negative of the comet's heliocentric velocity vector as seen in the plane of the sky is to the right for all images. Obvious dust coma was not detected in long exposures until $r \sim 3.1$ AU pre-perihelion, and dust was no longer visible in deep exposures after $r \sim 4.0$ AU post-perihelion.

effective sublimating ice surface area equal to about 1% at perihelion. A'Hearn et al. (1995) found a peak production rate of $Q_{OH} = 2 \times 10^{28}$ mol s^{-1} , corresponding to a 5.24 km² active area. Using the surface area determined by Thomas et al. (2007) from the encounter shape model of 119 km², this gives $f_{active} \sim 4.4\%$. A peak production rate for the 2005 apparition of $Q_{OH} = 6 \times 10^{27}$ mol s^{-1} , was about a factor of two less at perihelion (Schleicher, 2007). The peak 2005 production corresponded to $f_{active} \sim 1.8\%$. The dust production at perihelion fit with the simple water-sublimation models yields $\sim Q_{OH} = 1.7 \times 10^{27}$ mol s^{-1} and $f_{active} \sim 1\%$, which is consistent with the other data, given the accuracy of our model.

From the models, the dust production appears as a noticeable brightening in the light curve around $r \sim 4$ AU, inbound, and has stopped by $r \sim 4.6$ AU, outbound. Fig. 18 presents images of the comet over a range of distances over several apparitions to ascertain when the activity is evident from the images. All the images have been rotated in this figure so that the projected direction along the orbit is in the $+x$ -direction. The comet appears point-like with no obvious coma (even when doing surface brightness profiles) until between $r \sim 3.2$ – 3.1 AU, inbound. On the right side of the figure, there is substantial dust out until at least $r \sim 3.9$ AU, but much of the dust is along the orbit and may consist of large grains from perihelion (there is in fact, a hint of this large dust trail in the images out to $r \sim 4.2$ AU, outbound). The FP dust models show that at perihelion dust as large as mm-sized grains is lifted from the surface, and the water model is also consistent with maximum grains as large as mm-scale being lifted by the gas flow.

Ferrín (2007) discusses the light curve of 9P/Tempel 1 from a compilation of data from 1972–2005. After accounting for observing geometry, he noted an excess brightening near $r = 3.47 \pm 0.05$ AU (or -410 ± 25 days) pre-perihelion that he attributed to the onset of activity. Similarly, he inferred that activity ended near $r = 4.24 \pm 0.05$ AU (or $+555 \pm 25$ days). The activity profile obtained from our measurements indicates larger distances for activity onset and cessation of the comet. It also suggests that the approach of mathematical extrapolation and interpolation applied by Ferrín (2007) in order to estimate the distance range of onset and cessation can result in predictions deviating from reality because of the physical behavior of the comet. Table 8 summarizes the points in the orbit when the comet is active based on the light curves, FP dust modeling, appearance of coma and detectable gas. Clearly, a stellar-like cometary appearance is *not* a good indication that there

Table 8
9P/Tempel 1 activity.

Technique	Ref.	Onset–(r) (AU)	Onset– (time) (q–dys)	Cessation– (r) (AU)	Cessation– (time) (q+dys)
Light curve	1	-3.47 ± 0.05	-410 ± 25	$+4.24 \pm 0.05$	$+555 \pm 25$
FP models	2	> -3.2	> -350	–	–
H ₂ O sublimation	2	-4.0 ± 0.2	-580 ± 100	$+4.6 \pm 0.1$	$+780 \pm 200$
Coma appearance	2	-3.2	-350	$> +3.9$	$> +510$
CN detection	2	-2.43	-212	–	–

1 – Ferrín (2007), 2 – This paper.

is no activity, and the most sensitive way to detect activity is through monitoring the heliocentric light curve.

One interesting aspect of the water models seen in Table 7 is that the fractional active area (for water sublimation) had to increase to be consistent with the data; in other words, there were flat portions in the outbound light curve which were not fading fast enough to be explained by the sublimation model without increasing the effective active sublimation area. One possibility is that there is a seasonal effect causing the apparent increase in activity. Fig. 19 is a plot of the subsolar latitude for the nucleus illumination both pre- and post-perihelion. Using this, and checking the 3D shape model for the illumination geometry during the post-perihelion arc, in particular around 2.5 and 4 AU where the slope changes in the activity, it is difficult to argue that the activity profile is due to seasonal effects. The nucleus rotation axis is almost perpendicular to the orbital plane, which means that most of the nucleus is illuminated over a full rotation period and along the outbound arc of the orbit. It is possible that there was a significant decrease of water sublimation around 2.5 AU outbound and another volatile, say CO₂, became more dominant at about the same distance. This is plausible based upon the fact that the illumination conditions of the south polar region where the CO₂ activity was seen around perihelion (Feaga et al., 2007), and continuous day and night time dust emission was measured from the ground (Vincent et al., 2010), improve when the comet moves outbound. There is also likely a significant effect of thermal inertia. These processes can be more fully explored in a later paper with more detailed models.

Vasundhara (2009) discusses a detailed model of active nucleus source regions from dust images taken near the 2005 perihelion. Her models suggest several primary active regions on the surface, and that one of these is likely driven by CO₂ sublimation. The outbound heliocentric light curve may also have contributions from the various active regions as the illumination geometry changes. In order to understand the outbound light curve, a more detailed thermal model combined with a precise definition of the active regions is required, and this will be the subject of a subsequent paper.

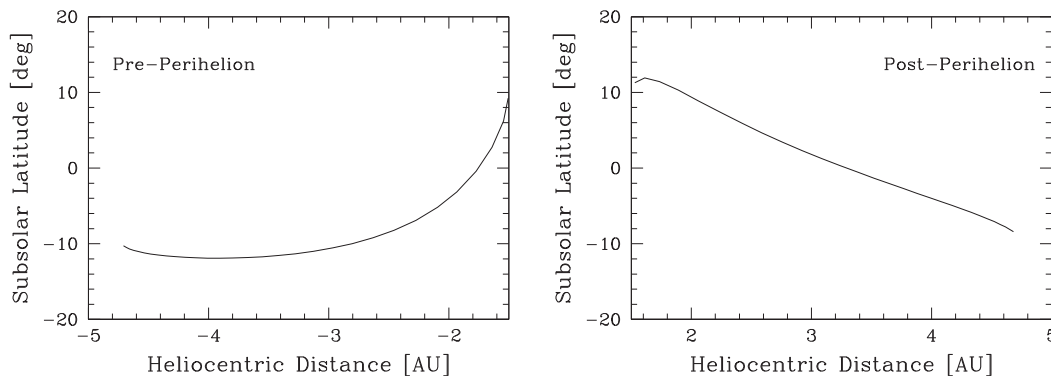


Fig. 19. Subsolar latitude for the nucleus illumination geometry pre- and post-perihelion for the 2005 apparition.

3.3. Direct detection of gas

From early December 2004 to early June 2005, we spectroscopically monitored the onset and the development of gaseous species (such as CN, C₂, C₃ and OH) in the coma of 9P/Tempel 1. The development of the gaseous species is shown in Fig. 13. In December 2004, 9P/Tempel 1 was at $r = 2.44$ AU from the Sun and the imaging data show that the cometary activity of 9P/Tempel 1 was still low. However, a weak CN emission band centered at 3880 Å was detected at a 10 σ level against the continuum. As the heliocentric distance of the comet approached $r = 2.1$ AU in January 2005, the CN emission band became at least 10 times stronger compared with the December data. In addition, a C₃ emission band was detected at 6 σ level and a C₂ emission band was detected at 4 σ level. In June 2005, the comet was only 1.5 AU from the Sun. As such, several strong emission bands were observed in the Jun data. In particular, an OH band at 3080 Å and a NH band at 3350 Å were detected. Although the OH band was strong, this is very near the edge of the chip which was not well flattened, and the flux of the standard stars were only measured to 3200 Å. In addition, the OH flux is also affected by the high and unknown near-UV extinction. The production rates are presented in Table 9.

The production rate of CN in December 2004 is relatively low compared with other comets at similar distances; however many of the comets with CN observed out to much larger distances are unusually active or dynamically new comets, and only a handful of Jupiter-family comets have had CN observed at distances as large as $r = 2.4$ AU (A'Hearn et al., 1995; Schulz and Schwehm, 1999; Schulz et al., 2004; Gilbert et al., 2010).

3.4. Secular variations

Low spectral resolution observations of the comet during four apparitions from 1983 through 2005 showed a secular decrease in gas production by a factor of 1.3–2.7, depending on the species (Cochran et al., 2009), with a peak in the production occurring roughly two months pre-perihelion. A similar secular decrease

Table 9

9P/Tempel 1 production rates.

Date	T^a	r (AU)	Δ (AU)	$\log Q(\text{CN})^b$	$\log Q(\text{C}_3)^b$	$\log Q(\text{C}_2)^{b,c}$	$\log Q(\text{NH})^b$	$\log Q(\text{OH})^{b,d}$
2004 December 4	-212	2.435	2.434	23.25 ± 0.20	—	—	—	—
2005 January 6	-180	2.241	1.850	23.44 ± 0.15	23.00 ± 0.25	23.28 ± 0.25	—	—
2005 June 8	-27	1.531	0.781	24.97 ± 0.15	24.76 ± 0.15	24.94 ± 0.20	25.51 ± 0.25	27.60 ± 0.25

^a Days before perihelion.

^b Production rate in mol s⁻¹.

^c For $\Delta v = 0$.

^d The error bars reflect the degree of the scatter in the data from the Haser model. The derived production rate of OH has a higher degree of uncertainty due to the large uncertainty in the flux measurement.

was seen in narrow band photometric data from 1983–2005 covering three apparitions (Schleicher, 2007). The decrease in the dust production was about 20% from 1994–2005, with larger variations in the gas species. Schleicher (2007) suggests that the very large decrease may indicate that the comet has at least two source regions of different compositions, one being near a rotation pole, and that one of these is becoming significantly less active.

The simple water models presented here (see Table 7 and Fig. 17) are also consistent with a secular decrease in water production of a factor of ~ 1.3 from the 2000 to the 2005 apparitions. Unfortunately, because every other apparition is poorly placed for ground-based observations, there will not be any additional pre-perihelion data for the 2011 apparition. Perihelion occurs on January 11, 2011, and the *Stardust-NEXT* encounter will be on February 14, 2011. At this time the comet will just barely be coming out of solar conjunction in the early morning twilight hours, and it will be difficult to observe from Earth until June 2011, at which point the comet will be near $r = 2.0$ AU outbound.

4. Conclusions

A massive, international observation program was carried out in support of the *Deep Impact* and *Stardust-NEXT* missions. Photometric data from 25 telescopes at 14 observatories were converted to a single photometric system based on the Kron–Cousins system on the UH 2.2-m telescope. The resulting light curve was a critical component of the mission allowing the behavior of the comet before, during, and after impact by the *Deep Impact* impactor spacecraft to be placed into context of evolving dust coma. The onset of dust production and its relationship to the beginning of water production were tracked during multiple apparitions of the comet. Early results were used to calculate exposure times for the DI impactor and flyby spacecraft. Temporal activity driven by dust ejection was monitored and the rotation of the nucleus was determined and this has been used to adjust the time of arrival of the *Stardust-NEXT* spacecraft (Belton et al., 2011).

In addition, from these data we have drawn the following conclusions:

1. We have determined the linear phase coefficient for the nucleus of the comet in the R-band to be 0.045 ± 0.001 over a range of phase angles from 1° to 16° when the comet was beyond $r = 4$ AU. This is in agreement with the linear phase coefficient seen for the resolved spacecraft images and is consistent with the linear phase functions of other low albedo comet nuclei.
2. Simple water-ice sublimation models can be made to fit the data which show that the effective fractional area of the nucleus that is active is $\sim 1\%$. Detectable activity began around 4.0 ± 0.2 AU ($q - 580 \pm 100$ dy), and ceased near $r = 4.6 \pm 0.1$ AU ($q + 780 \pm 200$ dy). The peak production rate of water implied by this model is $Q_{H_2O} \sim 2 \times 10^{27}$ mol s^{-1} , which is within reasonable agreement (factor of three) with perihelion measurements, given the approximations in the model.
3. Detectable extended dust coma in the images is not seen until $r \sim 3.1$ AU inbound for the 2000 apparition, but begins sometime between $r \sim 3.5$ and 2.5 AU for the 2005 apparition and between $r \sim 3.1$ and 2.8 AU for the 2011 apparition; thus the appearance of an extended dust coma is not a good indicator of early activity. The comet will typically be active at much larger heliocentric distances, but the coma beyond the seeing disk has a surface brightness below the detection threshold, even for very deep images.
4. There is a significant asymmetry in the heliocentric light curve. The maximum grain sizes coming off the surface when the activity began were a few microns in size and at perihelion up to mm size.
5. Finson–Probstein dust-dynamical models of pre-perihelion data from the 2000 apparition show that the inbound activity began prior to $q - 350$ days ($r > 3.7$ AU), with ejection of relatively small dust grains ($a \sim \text{few} - 30 \mu\text{m}$). This is consistent with the beginning of activity seen from the water-sublimation models. Post-perihelion models showed that the tail was consistent with the presence of grains as large as mm-sizes.
6. In order to fit the data, the effective fractional nucleus active area in the water-ice sublimation model for the outbound leg systematically increases between ~ 2 and 3.4 AU. This is unlikely to be caused only by a seasonal effect but may be caused by sublimation from active regions of different composition as the illumination geometry changed post-perihelion combined with thermal inertia effects. This will be addressed with more detailed modeling in a subsequent paper.
7. The activity on the inbound portion of the light curve shows a secular decrease in production of about a factor of 20% from the 2000 to the 2005 apparitions.
8. Monte-Carlo models of the dust jets seen near perihelion suggest that dust from the southern jet is ejected at low velocity (20 m s^{-1}) and may represent fluffy grains.
9. We present the earliest detection of CN gas in Comet 9P/Tempel 1 at a distance of $r = 2.435$ AU (December 4, 2004) with $Q(\text{CN}) = 1.8 \times 10^{23}$ mol s^{-1} . This was long after the first indications of activity from visible dust coma and the brightening seen in the heliocentric light curve. At $r = 2.241$ AU C_2 and C_3 emissions were detectable and $Q(\text{CN})$ had increased to 2.75×10^{23} mol s^{-1} and by June 6, 2005 at $r = 1.531$ AU, $Q(\text{CN})$ was at 9.3×10^{24} mol s^{-1} . This emphasizes the fact that going after spectroscopic detection of gas emission is not the most sensitive indication that activity has begun (because of sensitivity and resolution limitations); a measurement of the heliocentric light curve is more sensitive.

More detailed exploration of the data is currently under analysis, including:

1. We have datasets obtained during three oppositions when there was no apparent dust coma around the nucleus and when the comet passed through minimum phase angle (8/19/01–1/17/02, $14.1^\circ < \alpha < 1.3^\circ$; 10/12/03–1/2/04, $13.6^\circ < \alpha < 1.8^\circ$; 8/19/07–11/21/07, $12.7^\circ < \alpha < 0.5^\circ$). Careful modeling of these data will be performed to derive detailed information about the nucleus phase function and scattering properties of the surface materials comparing this with data obtained *in situ* from the spacecraft during encounter at very large phase angles. We now have sufficient knowledge of the rotation light curve (Belton et al., 2011) to remove the rotation signature from the data to search for an opposition surge and use Hapke modeling formalism.
2. We will compute more sophisticated thermal models accounting for multiple surface active regions of possibly differing composition, a changing particle size distribution and using quasi 3D code with input boundary constraints from the Finson–Probstein dust-dynamical models to study the activity and secular evolution of the nucleus.

Acknowledgments

This massive project would not have been possible without the support of observatory staff, support astronomers and the telescope operators. We would like to thank the UH2.2-m support staff who were a great help with the observations Lance Amano, Don De Cleene, John Dvorak, Paul Degrood, Chris Herrick, Chuck Sorenson,

Ian Renaud-Kim, Daniel Birchall, Greg Osterman, Richard Moriarty, John Archambeau, Dave Brennen, Avi Fhima, Don Weir, Cesar Nicolas, Callie McNew, Ed Sousa, and Andrew Pickles. We especially thank the UH2.2-m director Colin Aspin for all his support. In addition we thank the observers at the Purple Mountain Observatory Renquan Hong and Longfei Hu. We would also like to thank the observers who generously got an image of the comet for us, or a calibration field: Brian Barris (Northrup Grumman), Aaron Evans (University of Virginia), Chad Trujillo (Gemini Telescope). We especially thank Cedric Foellmi, science operations leader and Jorge Miranda the TO at La Silla, and Sangeeta Malhotra who took a few data points on the NTT 3.6-m and the CTIO4-m telescopes in Chile on short notice when Mauna Kea closed during the December 2003 blizzard. We thank Robert Gilmozzi, the Science Operations director at Paranal who awarded us the VLT time during January 2004. L.M. Lara is grateful to Chris Benn for acquiring some of the data. We especially thank Larry Wasserman for contributing data from several observing runs, and for his extensive help with setup and training at the Lowell 1.8-m telescope. We also gratefully thank support astronomer Chris Benn at the WHT who filled in when L. Lara became ill and could not observe. We thank the staff of IAO, Hanle and CREST, Hosakote, that made these observations possible. The facilities at IAO and CREST are operated by the Indian Institute of Astrophysics, Bangalore.

This material is based upon work supported by the National Aeronautics and Space Administration through the NASA Astrobiology Institute under Cooperative Agreement No. NNA04CC08A issued through the Office of Space Science, by NASA Grant Nos. NAGW 5015, NAG5-4495, NNX07A044G, NNX07AF79G, NASA STScI HST-GO-11887.01A, Cornell subcontract 51326-8653 (*Stardust-NExT*), and through the US-Israel Bi-national foundation (BSF) and by the Israel Ministry of Science, through the Israel Space Agency. D. Polishook acknowledges an Ilan Ramon Doctoral Fellowship from the Israel Space Agency. J. Pittichova was supported, in part, by the Scientific Grant Agency VEGA of the Slovak Academy of Science, 2/7040/27. J. Licandro acknowledges funding from the National Plan of I+D+i Project AYA2008-06202-C03-02 of the Spanish Ministry of Science and Innovation. B. E. A. Mueller, N. Samarasinha and T. Farnham were supported by NASA Grant NNG06G141G. This is PSI contribution 498. H. Zhao acknowledges the support by the National Natural Science Foundation of China (Grant Nos. 1050313 and 10933004) and the Minor Plant Foundation of Purple Mountain Observatory. Support for H. Hsieh was provided through STFC Fellowship Grant ST/F011016/1, and by NASA through Hubble Fellowship Grant HST-HF-51274.01A awarded by the Space Telescope Science Institute, which is operated by the Association of Universities for Research in Astronomy, Inc., for NASA, under Contract NAS 5-26555.

This is based in part on observations obtained at the Kitt Peak National Observatory, the Cerro Tololo Inter-American Observatory, National Optical Astronomy Observatory and the Gemini Observatory, which are operated by the Association of Universities for Research in Astronomy, Inc., under a cooperative agreement with the NSF on behalf of the Gemini partnership: the National Science Foundation (United States), the Science and Technology Facilities Council (United Kingdom), the National Research Council (Canada), CONICYT (Chile), the Australian Research Council (Australia), Ministério da Ciência e Tecnologia (Brazil) and SECYT (Argentina). The data are also based in part on observations obtained at the La Silla Paranal observatory of the European Southern Observatory, ESO. Telescope time was granted at Lowell Observatory through the PREST program, NSF Grant NSF04-557. This paper includes data taken at The McDonald Observatory of The University of Texas at Austin. This work is based in part on observations made with the WHT operated on the island of La Palma by the Isaac Newton Group in the Spanish Observatorio del Roque de los

Muchachos of the Instituto de Astrofísica de Canarias. This work is based in part on observations obtained at the La Silla – Paranal observatory of the European Southern Observatory ESO in Chile. Data were obtained in part from the Liverpool Telescope which is operated on the island of La Palma by Liverpool John Moores University in the Spanish Observatorio del Roque de los Muchachos of the Instituto de Astrofísica de Canarias with financial support from the UK Science and Technology Facilities Council.

Image processing in this paper has been performed using the IRAF software. IRAF is distributed by the National Optical Astronomy Observatories, which is operated by the Association of Universities for Research in Astronomy, Inc. (AURA) under cooperative agreement with the National Science Foundation.

Appendix A. Supplementary material

Supplementary data associated with this article can be found, in the online version, at doi:10.1016/j.icarus.2011.02.016. This includes descriptions of all of the observing runs and a table which shows the observing geometry and observing conditions for each night of observation.

References

- A'Hearn, M.F. et al., 2005. Deep Impact: Excavating Comet Tempel 1. *Science* 310, 258–264.
- A'Hearn, M.F., Millis, R.L., Schleicher, D.G., Osip, D.J., Birch, P.V., 1995. The ensemble properties of comets: Results from narrowband photometry of 85 comets. *Icarus* 118, 223–260.
- Belton, M.J.S. et al., 2005. Deep Impact: Working properties for the target nucleus – Comet 9P/Tempel 1. *Space Sci. Rev.* 117, 137–160.
- Belton, M.J.S., Melosh, J., 2009. Fluidization and multiphase transport of particulate cometary material as an explanation of the smooth terrains and repetitive outbursts on 9P/Tempel 1. *Icarus* 200, 280–291.
- Belton, M.J.S. et al., 2011. Stardust-NExT, Deep Impact, and the accelerating spin of 9P/Tempel 1. *Icarus*, in press. doi:10.1016/j.icarus.2011.01.006.
- Cochran, A.L., Schleicher, D.G., 1993. Observational constraints on the lifetime of cometary H₂O. *Icarus* 105, 235–253.
- Cochran, A.L., Barker, E.S., Ramseyer, T.F., Storrs, A.D., 1992. The McDonald Observatory faint comet survey – Gas production in 17 comets. *Icarus* 98, 151–162.
- Cochran, A.L., Barker, E.S., Cabellero, M.D., Gyorgy-Ries, J., 2009. Placing the Deep Impact mission into context: Two decades of observations of 9P/Tempel 1 from McDonald observatory. *Icarus* 199, 119–128.
- Cowan, J.J., A'Hearn, M.F., 1982. Vaporization in comets: Outbursts from Comet Schwassmann–Wachmann 1. *Icarus* 50, 53–62.
- Davidsson, B.J.R., Gutierrez, P.J., Rickman, H., 2007. Nucleus properties of Comet 9P/Tempel 1 estimated from non-gravitational force modeling. *Icarus* 187, 306–320.
- Farnham, T.L., 1996. Modeling cometary dust tails with a pseudo-Finson–Probstein technique. Ph.D. Thesis, University of Hawaii.
- Farnham, T.L. et al., 2007. Dust coma morphology in the Deep Impact images of Comet 9P/Tempel 1. *Icarus* 187, 26–40.
- Feaga, L.M., A'Hearn, M.F., Sunshine, J.M., Groussin, O., Farnham, T.L., 2007. Asymmetries in the distribution of H₂O and CO₂ in the inner coma of Comet 9P/Tempel 1 as observed by Deep Impact. *Icarus* 190, 345–356.
- Feldman, P.D. et al., 2007. Hubble Space Telescope observations of Comet 9P/Tempel 1 during the Deep Impact encounter. *Icarus* 187, 113–122.
- Fernández, Y.R. et al., 2003. The nucleus of Deep Impact target Comet 9P/Tempel 1. *Icarus* 164, 481–491.
- Ferrín, I., 2007. Secular light curve of Comet 9P/Tempel 1. *Icarus* 191, 567–572.
- Finson, M.L., Probstein, R.F., 1968. A theory of dust comets. I. Model and equations. *Astrophys. J.* 154, 327–352.
- Gilbert, A.M., Wiegert, P.A., Unda-Sanzana, E., Vaduvescu, O., 2010. Spectroscopic observations of new Oort cloud Comet 2006 VZ13 and four other comets. *Mon. Not. R. Astron. Soc.* 401, 2399–2405.
- Groussin, O. et al., 2007. Surface temperature of the nucleus of Comet 9P/Tempel 1. *Icarus* 187, 16–25.
- Haser, L., 1957. Distribution d'intensité dans la tête d'une comète. *Bull. Soc. R. Sci. Liège* 43, 740–750.
- Lamy, P.L., Toth, I., A'Hearn, M.F., Weaver, H.A., Weissman, P.R., 2001. Hubble Space Telescope observations of the nucleus of Comet 9P/Tempel 1. *Icarus* 154, 337–344.
- Lamy, P.L., Toth, I., A'Hearn, M.F., Weaver, H.A., Jorda, L., 2007. Hubble Space Telescope observations of Comet 9P/Tempel 1 during the Deep Impact encounter. *Icarus* 187, 337–344.
- Landolt, A.U., 1992. UBVR photometric standard stars in the magnitude range 11.5–16.0 around the celestial equator. *Astron. J.* 104, 340–371. 436–491.

- Lara, L.M. et al., 2006. Pre-impact monitoring of Comet 9P/Tempel 1, the Deep Impact target. *Astron. Astrophys.* 445, 1151–1157.
- Lara, L.M. et al., 2007. Behavior of Comet 9P/Tempel 1 around the Deep Impact event. *Astron. Astrophys.* 465, 1061–1067.
- Li, J.-Y. et al., 2007. Deep Impact photometry of Comet 9P/Tempel 1. *Icarus* 187, 41–55.
- Lisse, C.M. et al., 2005. The coma of Comet 9P/Tempel 1. *Space Sci. Rev.* 117, 161–192.
- Lisse, C.M. et al., 2006. Spitzer spectral observations of the Deep Impact ejecta. *Science* 313, 635–640.
- Meech, K.J. et al., 2004. The Deep Impact Earth-based campaign. *SSR* 117, 297–334.
- Meech, K.J. et al., 2005. Deep Impact: Observations from a worldwide Earth-based campaign. *Science* 310, 265–269.
- Meech, K.J., Jewitt, D., Ricker, G.R., 1986. Early photometry of Comet P/Halley: Development of the coma. *Icarus* 66, 561–574.
- Meech, K.J., Wilson, L., Pralnik, D., 2008. Smooth regions on Comet 9P/Tempel 1: Cryovolcanic emplacement? *LPI Contrib.* 1405, 8341.
- Mumma, M.J. et al., 2005. Parent volatiles in comet 9P/Tempel 1: Before and after impact. *Science* 310, 270–274.
- Randall, C.E., Schleicher, D.G., Ballou, R.G., Osip, D.J., 1992. Observational constraints on molecular scalelengths and lifetimes in comets. *Bull. Am. Astron. Soc.* 24, 1002.
- Richardson, J.E., Melosh, H.J., Lisse, C.M., Carcich, B., 2007. A ballistics analysis of the Deep Impact ejecta plume: Determining Comet Tempel 1's gravity, mass and density. *Icarus* 187, 41–55.
- Samarasinha, N.H., Schleicher, D.G., Woodney, L.M., 2004. Modeling CN jets of comet Hyakutake (C/1996B2). *BAAS* 36, 1146.
- Schleicher, D.G., 2007. Deep Impact's target Comet 9P/Tempel 1 at multiple apparitions: Seasonal and secular variations in gas and dust production. *Icarus* 190, 406–422.
- Schulz, R., Schwehm, G., 1999. Coma composition and evolution of Rosetta target Comet 46P/Wirtanen. *Space Sci. Rev.* 90, 321–328.
- Schulz, R., Stüwe, J.A., Boehnhardt, H., 2004. Rosetta target Comet 67P/Churyumov–Gerasimenko. Postperihelion gas and dust production rates. *Astron. Astrophys.* 422, L19–L21.
- Sunshine, J.M. et al., 2006. Exposed water ice deposits on the surface of Comet 9P/Tempel 1. *Science* 311, 1453–1455.
- Thomas, P.C. et al., 2007. The shape, topography, and geology of Tempel 1 from Deep Impact observations. *Icarus* 187, 4–15.
- Tody, D., 1986. The IRAF data reduction and analysis system. In: Crawford, D.L. (Ed.), *SPIE Instrumentation in Astronomy VI*, vol. 627, pp. 733–748.
- Vasundhara, R., 2009. Investigations of the pre-Deep Impact morphology of the dust coma of Comet Tempel 1. *Icarus* 204, 194–208.
- Vincent, J.-B., Boehnhardt, H., Lara, L.M., 2010. A numerical model of cometary dust coma structures. Application to Comet 9P/Tempel 1. *Astron. Astrophys.* 512, 60–68.
- Yeomans, D., Giorgini, J., Chesley, S., 2005. History and dynamics of Comet 9P/Tempel 1. *Space Sci. Rev.* 117, 123–135.